Ocean Engineering 353 (2026) 124746

Contents lists available at ScienceDirect

Ocean Engineering

journal homepage: www.elsevier.com/locate/oceaneng

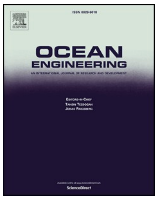

Research paper

Self-starting characteristics and dynamic response of a free-spinning cross-flow air turbine for oscillating water columns under irregular wave conditions

B.H.B.P.D. Baddegamage [a,b], Seong Jong Bae [a,b], S.D.G.S.P. Gunawardane [c], Young-Ho Lee [d], Kilwon Kim [e], Min Yoon [a,b,*]

[a] *Department of Mechanical Engineering, Korea Maritime & Ocean University, Busan, 49112, Republic of Korea*
[b] *Interdisciplinary Major of Ocean Renewable Energy Engineering, Korea Maritime & Ocean University, Busan, 49112, Republic of Korea*
[c] *Department of Mechanical Engineering, Sri Lanka Institute of Information Technology (SLIIT), Malabe, 10115, Sri Lanka*
[d] *Center for Offshore Wind and Green Hydrogen Ammonia Research, Korea Maritime & Ocean University, Busan, 49112, Republic of Korea*
[e] *Ocean Plant Research Division, Korea Research Institute of Ships and Ocean Engineering, Daejeon, 34103, Republic of Korea*

ARTICLE INFO

Keywords:
Cross-flow air turbine
Oscillating water columns
Irregular waves
Self-starting behavior
Computational fluid dynamics
Wave energy

ABSTRACT

The cross-flow air turbine (CFAT) has been proposed as a self-rectifying device for oscillating water column (OWC) wave energy converters as an alternative to conventional Wells and impulse turbines. While previous studies have primarily focused on steady or regular flow conditions, the self-starting behavior and transient response of a free-spinning CFAT under irregular, bidirectional inflow representative of realistic sea states have not yet been investigated. This study presents a fully transient computational fluid dynamics analysis of a free-spinning CFAT operating under irregular airflow conditions derived from the JONSWAP spectrum. The simulations were performed under no-load conditions to isolate the intrinsic aerodynamic torque generation and evaluate self-starting capability. The effects of significant wave height and spectral peak period on turbine startup and unsteady aerodynamic response were systematically examined in both the time and frequency domains. The CFAT consistently initiates rotation without external assistance and reaches quasi-steady operation within 25–30 oscillation cycles. For significant wave heights ranging from 0.0375 m to 0.05 m, the mean instantaneous efficiency varies between 0.24 and 0.52, while efficiencies between 0.30 and 0.59 are obtained for spectral peak periods from 1.50 s to 1.88 s. Furthermore, wave-grouping effects play a decisive role in accelerating the turbine toward its equilibrium speed. Torque and pressure fluctuations closely follow the inflow velocity profile, with hysteresis-like behavior observed during flow reversals. These findings confirm the CFAT's suitability for practical OWC applications, demonstrating robust self-starting and stable performance under irregular conditions.

Nomenclature

Symbol	Description	Unit
Romans		
A_c	Cross-sectional area of OWC air chamber	m^2
D_1	Rotor outer diameter	m
D_2	Rotor inner diameter	m
g	Gravitational acceleration	m/s^2
H	Incident wave height	m
H_s	Significant wave height	m
h	Instantaneous water surface elevation inside chamber	m
I	Rotor moment of inertia	kg·m^2
k	Turbulent kinetic energy	m^2/s^2
p	Mean static pressure	Pa
Δp	Pressure drop across turbine	Pa
Δp_c	Air pressure variation inside OWC chamber	Pa
P_W	Wave energy flux per unit crest length	W/m
P_{pneu}	Pneumatic power	W
P_{turb}	Turbine power	W
Q	Volumetric airflow rate	m^3/s
t	Time	s
t^*	Normalized time (t/T_p)	-

(*continued on next page*)

---

* Corresponding author. Department of Mechanical Engineering, Korea Maritime & Ocean University, Busan, 49112, Republic of Korea.
E-mail address: minyoon@kmou.ac.kr (M. Yoon).

https://doi.org/10.1016/j.oceaneng.2026.124746
Received 11 November 2025; Received in revised form 22 January 2026; Accepted 17 February 2026

(*continued*)

T_D	Aerodynamic driving torque	N·m
T_L	External loading torque	N·m
T_e	Wave energy period	s
T_p	Peak spectral wave period	s
T_{turb}	Turbine torque	N·m
U	Mean airflow velocity	m/s
u_i	Velocity fluctuation component	m/s
x_i	Cartesian coordinate	m
y^+	Non-dimensional wall distance	-
Greek symbols		
α	Nozzle angle of attack	°
β_1	Blade inlet angle	°
β_2	Blade exit angle	°
γ	Nozzle starting angle	°
γ_1	Skewness	-
ε	Turbulent dissipation rate	m^2/s^3
η	Turbine efficiency	-
η^*	Mean instantaneous efficiency	-
λ	Nozzle entry arc angle	°
μ	Dynamic viscosity	Pa·s
μ_t	Turbulent viscosity	Pa·s
Π	Torque coefficient	-
ρ	Air density	kg/m^3
ρ_w	Water density	kg/m^3
σ	Standard deviation	-
Φ	Flow coefficient	-
Ψ	Pressure coefficient	-
Ω	Rotor angular velocity	rad/s
ω	Specific turbulent dissipation rate	1/s
ω_p	Peak angular wave frequency	rad/s
Superscripts		
*	Instantaneous value	
-	Time-averaged value	
Acronyms		
3D	Three-dimensional	
CFAT	Cross-flow air turbine	
CFD	Computational fluid dynamics	
JONSWAP	Joint North Sea Wave Project	
OWC	Oscillating water column	
PSD	Power spectral density	
SST	Shear stress transport	
TKE	Turbulence kinetic energy	
URANS	Unsteady Reynolds-averaged Navier–Stokes	

1. Introduction

Wave energy, driven by wind as a by-product of the atmosphere's redistribution of solar radiation, was recognized as a potential source of electricity following the renewed interest in ocean waves as a renewable resource that emerged during the 1973 oil crisis (Cruz, 2007; Falcão, 2025). Compared to other renewable energy sources, wave energy offers distinct advantages, including higher energy density and greater predictability (Ding et al., 2025; Veigas et al., 2014). Among the various technologies developed for wave energy conversion, oscillating water column (OWC) wave energy converters (WECs) are notable for their structural simplicity and operational reliability (Doyle and Aggidis, 2019; Heath, 2012). Fixed OWC systems, in particular, benefit from having few or no moving parts in contact with seawater, which results in lower maintenance demands. This robustness, combined with minimal mechanical exposure to harsh marine environments, makes OWCs an attractive option for long-term deployment.

In an OWC device, incident waves induce oscillations in a partially submerged water column enclosed within a chamber. These oscillations drive the air above the water surface in and out of the chamber, converting wave energy into pneumatic energy. The resulting airflow is directed through a duct to rotate a unidirectional air turbine, thereby transforming pneumatic energy into mechanical energy. Finally, the turbine drives a generator to produce electricity (Lyu et al., 2025; Qiao et al., 2020). The performance of an OWC-WEC is influenced by various factors, including wave conditions, tidal level, and the interaction between the chamber and the air turbine (López and Iglesias, 2014). In the case of a self-rectifying turbine, air flows between the chamber and the atmosphere, maintaining a consistent rotational direction regardless of the airflow direction (Curran and Folley, 2008; Falcão et al., 2018; Falcão and Henriques, 2016; Setoguchi et al., 2001). Several types of self-rectifying turbines have been developed for integration into OWC systems as the power take-off mechanism, including the Wells turbine (Shehata et al., 2017; Wells, 1976), axial-flow impulse turbine (Babintsev, 1975; Setoguchi et al., 1999), radial-flow impulse turbine (Pereiras et al., 2011), biradial turbine (Bae et al., 2026; Falcão et al., 2013a, 2013b), and twin rotor turbine (Lopes et al., 2019).

This study focuses on a self-rectifying cross-flow air turbine (CFAT), whose rotor is adapted from the cross-flow turbine commonly used in hydropower applications (Kang et al., 2017). The cross-flow turbine, also known as the Banki–Michell turbine, usually achieves a maximum efficiency of about 80%, with approximately 70–90% and 10–30% of the energy exchanged in the first and second stages, respectively (Quaranta et al., 2022). The CFAT comprises two main components: a stationary nozzle and a rotating runner. The nozzle accelerates and directs the inlet flow toward the runner, which the flow then traverses twice: upon entry and upon exiting through the central region. To accommodate bidirectional airflow, the CFAT employs a dual-nozzle configuration, with two identical nozzles symmetrically placed on opposite sides of the runner and mirrored about the turbine's central axis, as illustrated in Fig. 1. This arrangement ensures that airflow from either direction is effectively captured and directed through the runner, enabling consistent turbine rotation regardless of the flow direction. Although research on CFAT remains limited, initial computational studies demonstrated promising performance. Early numerical investigations assessed the feasibility of CFAT as an OWC air turbine (Wata and Lee, 2015; Wata et al., 2016). Building upon these efforts, Kang et al. (2022) conducted both numerical and experimental analyses using a cylindrical wave simulator and confirmed that CFAT offers structural simplicity and a wide operational range with high efficiency. More recently, Baddegamage et al. (2025) optimized the nozzle and blade geometry, performing numerical simulations that revealed peak efficiencies of 0.71 in steady flow and 0.68 under bidirectional sinusoidal flow. Notably, the turbine maintained stable performance across a broad range of operating conditions, with efficiency not dropping below 45% within the considered flow range.

Typically, the aerodynamic performance of air turbines is evaluated using steady-state or quasi-steady-state approaches (Liu et al., 2019). In steady-state analysis, the turbine is subjected to constant, unidirectional airflow, allowing performance to be assessed over a set of fixed operating points. The quasi-steady approach, by contrast, approximates unsteady inflow as a sequence of steady conditions, using time-varying flow inputs while relying on steady-state characteristics. These methodologies have been instrumental in guiding design improvements, particularly in blade geometry, tip clearance, and rotor–stator arrangements. However, quasi-steady models inherently neglect the influence of time-evolving effects such as transient variations in aerodynamic loads, delayed torque buildup, and inertial response during flow reversal (Cui et al., 2022). These dynamic responses become especially significant under reciprocating or irregular airflow patterns, which better represent realistic sea states. Thus, fully transient numerical simulations are essential for capturing the complete operational dynamics of air turbines within OWCs and for enhancing the accuracy of performance predictions under actual wave forcing before moving into the prototype stage.

This highlights the need for flow-driven transient simulations to evaluate turbine behavior under realistic OWC operating conditions. While many previous studies rely on sinusoidal inflow profiles, actual wave climate exhibits highly irregular, non-sinusoidal characteristics shaped by stochastic sea states and spectral complexity. Capturing such irregular flow patterns in simulations is vital to accurately assess turbine behavior, including self-starting capability, efficiency trends, and power smoothing, especially under conditions involving wave group

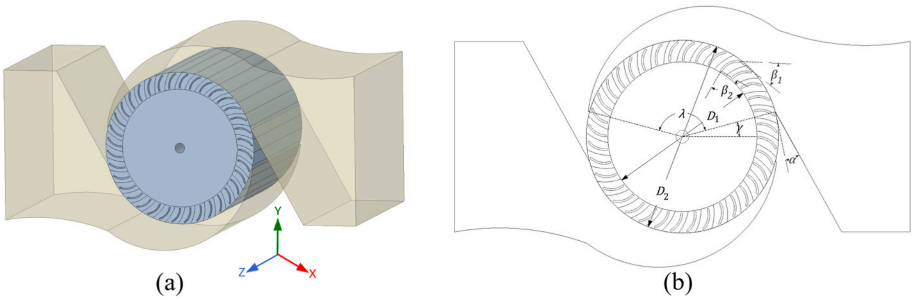

Fig. 1. (a) 3D representation of the CFAT depicting two symmetrical nozzles, the runner, and the shaft at the center. (b) 2D schematic diagram marking geometry parameters.

characteristics and spectral sea states (Setoguchi and Takao, 2006).

Self-starting capability has long been recognized as a critical challenge in turbine design, especially for lift-based rotors that generate insufficient starting torque at low tip-speed ratios. In the context of cross-flow wind turbines operating under unidirectional inflow, numerous studies have explored self-starting enhancement strategies, including auxiliary blades, blade pitch modification, and guide-vane-assisted configurations for both lift-based Darrieus turbines (Ghafoorian et al., 2024a) and drag-based Savonius turbines (Ghafoorian et al., 2024b). While these studies provide valuable insights into start-up behavior under steady or weakly unsteady wind conditions, the underlying mechanisms differ fundamentally from those governing air turbines in oscillating water column systems, where the inflow is inherently bidirectional, strongly unsteady, and intermittently driven by wave-induced pressure oscillations.

In OWC applications, several studies have employed CFD- and experiment-based approaches to investigate the dynamic behavior of various self-rectifying air turbines under irregular wave conditions. Liu et al. (2021) experimentally examined the overall performance of a model OWC system operating in free-spinning mode under irregular waves, demonstrating that impulse turbines retain reliable self-starting ability even in spectrum-based inflow conditions. Their results revealed that turbine rotational speed strongly affects chamber hydrodynamics and pneumatic performance, and that an optimal resonant significant wave period exists for maximizing primary-stage efficiency under free-spinning operation. Furthermore, they showed that secondary-stage efficiency can exceed that of forced-spinning cases over a range of load coefficients due to improved matching between turbine operation and incident pneumatic power. The same authors subsequently extended this work by developing a CFD-based wave-to-wire framework capable of predicting the coupled wave-chamber-turbine dynamics under both regular and irregular wave conditions (Liu et al., 2022). Complementary wave-flume experiments by Liu et al. (2018) further clarified that, under irregular waves, the overall efficiency trends of OWC systems are largely governed by the turbine operating speed, while the secondary-stage efficiency is comparatively insensitive to wave period but highly dependent on rotational control strategy. These findings collectively indicate that free-spinning turbine dynamics introduce strong coupling between wave excitation, chamber pressure response, and rotor inertia, which cannot be adequately captured by steady or forced-rotation assumptions.

In parallel, extensive numerical investigations have focused on Wells turbines under unsteady and irregular inflow conditions. Ghisu et al. (2015) performed numerical simulations of a Wells turbine under various flow conditions, and Hu and Li (2017) analyzed the steady and unsteady aerodynamic characteristics of a Wells turbine, considering two control strategies: constant angular velocity and constant damping moment, under unsteady inflow conditions. Cui et al. (2022) developed a three-dimensional (3D) transient CFD model to simulate the time-varying flow field and rotor motion of a Wells turbine during free-spinning operation and subsequently applied it to investigate operating patterns under different airflow profiles. More recently, Wang et al. (2024) focused on predicting the unsteady response of a free-spinning Wells turbine subjected to irregular wave conditions. In the context of axial impulse turbines, Liu et al. (2018) first developed a 3D transient model to evaluate unsteady rotor performance, and Cui et al. (2019) subsequently analyzed their self-starting capability under constant flows. Luo et al. (2022) conducted a comparative analysis on the influence of rotor moment of inertia, wave period, wave height, and air compressibility on the start-up process of the impulse turbine.

Despite this substantial body of work on Wells and axial impulse turbines, comparable investigations for CFATs remain scarce, particularly with respect to free-spinning operation driven by realistic, spectrum-derived inflow conditions. Moreover, most existing CFAT studies have focused on steady or prescribed inflow scenarios, leaving the combined effects of bidirectional flow reversal, short acceleration intervals, and inertial rotor dynamics largely unexplored.

The present study aims to investigate the starting behavior and the aerodynamic performance of a CFAT under no-load conditions under realistic, irregular wave-induced airflow conditions using fully transient CFD simulations. Irregular inflow profiles derived from an ocean wave spectrum are employed to capture the inherently bidirectional and strongly unsteady nature of OWC-driven airflow, evaluating the key performance metrics, including torque response, inlet–outlet pressure drop, angular velocity evolution, and instantaneous flow field characteristics. By focusing on free-spinning operation under spectrum-derived inflow conditions, this study explicitly addresses the lack of prior investigations into CFAT startup dynamics under realistic OWC operating scenarios, which cannot be adequately represented by steady or prescribed inflow assumptions. The study contributes to a more comprehensive understanding of CFAT dynamics in OWC systems and provides insights into its viability as a robust and efficient turbine for wave energy conversion in real-world operating conditions. Section 2 presents a detailed description of CFAT geometry, and the numerical model adopted in this study. It then introduces the free-spinning model and the generation of irregular waves. Section 3 discusses numerical results, with particular emphasis on startup characteristics under different irregular inflow profiles and the influence of wave parameters on CFAT performance. Finally, the main conclusions are provided in Section 4.

2. Methodology

2.1. *Cross-flow air turbine geometry*

The CFAT geometry remains unchanged from the optimized model used in our previous research (Baddegamage et al., 2025). As illustrated in Fig. 1a, CFAT consists of four distinct components: the rotor, the center shaft, and the two nozzles positioned on opposite sides of the runner and mirrored about the turbine's central axis. The rotor, with a diameter is 0.3 m, consists of thirty-six blades with a uniform cylindrical cross-section and a consistent thickness of 3 mm. More details on the turbine geometry are listed in Table 1. The relevant parameters are

Table 1
Detailed parameters of the turbine geometry.

Symbol	Quantity	Unit
D_1	Outer diameter	0.3 m
D_2	Inner diameter	0.24 m
-	Rotor and nozzle widths	0.04 m
-	Nozzle throat width ratio	0.38
-	Number of blades	36
-	Thickness of blades	3 mm
-	Tip clearance	2 mm
α	Angle of attack	14°
β_1	Blade inlet angle	26.5°
β_2	Blade exit angle	90°
λ	Nozzle entry arc angle	150°
γ	Nozzle starting angle	15°

marked in Fig. 1b.

2.2. Numerical model

The fluid domain was discretized using Ansys ICEM CFD 19.2, which comprised approximately 2 million elements. A grid-independence study was conducted by refining the mesh from 1.4 million to 3.4 million elements under uniform flow in steady-state conditions. The monitored torque varied by less than 0.1% beyond 2 million cells, indicating mesh convergence. Therefore, a mesh with approximately 2 million elements was adopted for all subsequent simulations to strike a balance between accuracy and computational efficiency. More detailed mesh specifications of the grid-independence study are shown in Table 2. A structured hexahedral mesh was employed, with a refined mesh used near the walls to enhance accuracy in solving the complex turbulent flow around the wall. The y^+ value, which represents the non-dimensional distance from the first grid cell to the surface wall, was maintained below 4 in the runner and the nozzle domain and below 5 in the inlet and outlet passage domains. The inlet and outlet faces were extended $5D_1$ away from the nozzle interfaces to provide sufficient distance to build up velocity, minimize their influence on the simulation results, and avoid recirculation issues. Fig. 2a shows the computational model, and Fig. 2b illustrates the numerical mesh highlighting the near-wall mesh refinement of the rotor.

Numerical simulations were conducted using Ansys CFX 19.2. Unsteady Reynolds-averaged Navier–Stokes (URANS) equation was employed in transient simulations. The shear stress transport (SST) k-ω model was utilized as the turbulence model. Here, k is the turbulent kinetic energy, and ω is the specific turbulent dissipation rate. The SST model has been widely used in turbomachinery as an analysis tool to investigate complex flow phenomena, including rotor-stator interactions, tip leakage, and flow separations (Balasubramanian et al., 2008). The SST model switches between the k-ε model in the free stream and the k-ω model near the wall region, which balances computational accuracy and cost (Lacombe et al., 2019; Menter et al., 2003). Here, ε denotes the turbulent dissipation rate. The governing URANS equations are as follows:

$$\frac{\partial \rho}{\partial t} + \frac{\partial(\rho U_j)}{\partial x_j} = 0 \tag{1}$$

$$\frac{\partial(\rho U_i)}{\partial t} + \frac{\partial(\rho U_i U_j)}{\partial x_j} = -\frac{\partial p}{\partial x_i} + \frac{\partial\left[\tau_{ij} - \rho\overline{u_i u_j}\right]}{\partial x_j} + S_M \tag{2}$$

where ρ is the air density, U_i denotes the mean velocity components, x_i represents the Cartesian coordinates, p is the mean static pressure, u_i denotes the velocity fluctuation components, τ_{ij} is the molecular stress tensor, and S_M represents the source terms associated with the rotating reference frame. The bar denotes the time average. The transport equations for turbulent kinetic energy and specific dissipation rate are:

$$\frac{\partial(\rho k)}{\partial t} + \frac{\partial(\rho U_j k)}{\partial x_j} = P_k - \beta' \rho k \omega + \frac{\partial}{\partial x_j}\left[\left(\mu + \frac{\mu_t}{\sigma_k}\right)\frac{\partial k}{\partial x_j}\right] + P_{kb} \tag{3}$$

$$\frac{\partial(\rho \omega)}{\partial t} + \frac{\partial(\rho U_j \omega)}{\partial x_j} = \alpha' \frac{\omega}{k} P_k - \beta \rho \omega^2 + \frac{\partial}{\partial x_j}\left[\left(\mu + \frac{\mu_t}{\sigma_\omega}\right)\frac{\partial \omega}{\partial x_j}\right] + P_{\omega b} \tag{4}$$

where P_k represents the production term of the turbulent kinetic energy, μ represents the dynamic viscosity, and μ_t represents the turbulent viscosity. β', α', β, σ_k, and σ_ω represent the model constants given in Menter (1994). P_{kb} and $P_{\omega b}$ are the additional buoyancy terms.

Table 2
Grid-independence study.

Grid properties	Grid 1	Grid 2	Grid 3	Grid 4	Grid 5	Grid 6
Number of elements (millions)	1.45	1.77	2.09	2.57	2.93	3.39
First layer thickness around blades [μm]	9.00	9.34	9.34	9.34	9.34	9.34
y^+	3.74	3.73	3.72	3.72	3.72	3.72
Growth rate	1.120	1.100	1.092	1.070	1.065	1.060
Averaged torque	4.419	4.429	4.445	4.446	4.448	4.448

In this study, air at 25 °C is considered as the working fluid and assumed to be incompressible since the Mach number barely exceeded 0.3 in the tested cases. The inlet boundary condition was defined as a velocity inflow, while the outlet was set using a pressure opening boundary condition with a relative pressure of 0 Pa. The simulations were conducted under atmospheric pressure. The additional boundary conditions are summarized in Table 3. The top and bottom boundaries functioned as walls, while the two adjacent surfaces in the spanwise direction were defined as symmetry, resulting in a quasi-3D configuration. A preliminary sensitivity analysis indicated that variations in spanwise length had a negligible influence on the results (Baddegamage et al., 2024). Hence, a spanwise length of 0.04 m was adopted to reduce computational cost. An adaptive timestep strategy is adopted, updating the time step every five iterations to control the root-mean-square Courant number. The fully implicit formulation of Ansys CFX ensures that the solver remains stable at relatively larger time steps, while the adaptive control improves convergence robustness under unsteady flow conditions. The baseline CFD model from Baddegamage et al. (2025) was validated against the experimental results of Kang et al. (2022).

2.3. Free-spinning model

To capture the realistic transient behavior of the CFAT subjected to reciprocating airflow, a fully unsteady free-spinning numerical model was developed using rigid body motion. Unlike conventional fixed-speed simulations that impose a constant angular velocity, the present numerical model allows the turbine rotor to rotate passively in response to the instantaneous torque induced by the bidirectional airflow. This approach enables the simulation of self-starting behavior, where the rotor initiates motion from rest and accelerates purely under the influence of the flow. The turbine's rotational dynamics are governed by Newton's second law of motion, modeled as a single degree-of-freedom system. The governing equation is expressed as:

$$I\frac{d\Omega}{dt} + T_L = T_D, \tag{5}$$

where I denotes the moment of inertia of the rotor, Ω is the angular velocity, T_D is the driving torque, and T_L represents the loading torque arising from generator resistance, mechanical friction, and other system losses. At each timestep, the driving torque is computed by integrating the surface pressure and shear forces acting on the rotor blades, each weighted by its distance from the axis of rotation. The resulting torque

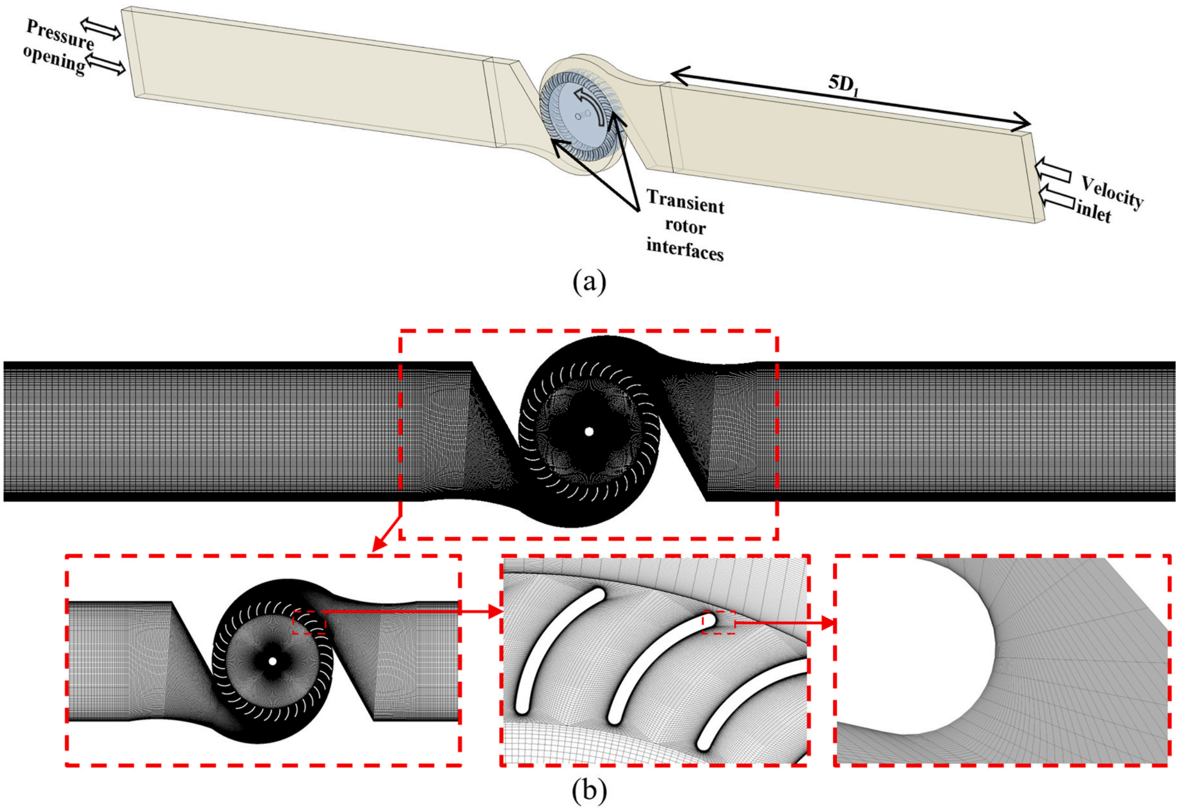

Fig. 2. (a) Computational domain and (b) numerical mesh emphasizing the refined cells near the walls of the turbine.

Table 3
Detailed boundary conditions of the numerical model.

Parameter	Value
Analysis type	Transient
Inlet	Varying velocity
Turbulence intensity	0.05
Viscosity ratio	10
Outlet	Opening
Time step	Adaptive (initially 0.001 s)
Simulation time	80 s
Mesh interface	Transient rotor stator

Table 4
Rigid body solution setup.

Parameter	Value
Mass of the rotor	1.004 kg
Mass moment of inertia	XX $= 0.00941974$ kg/m^2 YY $= 0.00941974$ kg/m^2 ZZ $= 0.01857180$ kg/m^2 XY $= 0$ XZ $= 0$ YZ $= 0$

determines the instantaneous angular acceleration, which is then used to update the angular velocity and blade position through a first-order backward Euler algorithm, as outlined in the CFX-solver theory guide (CFX-Solver ANSYS, 2019). This updated position modifies the surrounding flow field, which in turn influences the pressure distribution and torque in the subsequent timestep. Through this iterative process in the absolute reference frame, the model captures the flow-driven rotation of the turbine with full coupling between aerodynamic and rotational dynamics, thereby providing a realistic assessment of the turbine's unsteady performance and self-starting capability under irregular wave-induced airflows.

The rigid-body motion of the turbine rotor was defined by specifying its mass and inertial properties within the six-degree-of-freedom solver framework, with rotation permitted only about the principal axis of the shaft (z-axis) and all translational degrees of freedom constrained. The rotor mass, center of gravity, and principal moments of inertia were calculated based on the geometric and material properties of the turbine as listed in Table 4.

In this study, the CFAT was modeled under a no-load ($T_L = 0$) condition. This simplification intentionally isolates the aerodynamic response of the turbine from electrical damping effects, enabling a clearer examination of the intrinsic aerodynamic torque balance and the resulting transient behavior. Although this assumption deviates from the actual operating condition of OWC systems, where generator damping and mechanical friction impose non-negligible resistance, it allows the investigation of fundamental response characteristics such as equilibrium under aerodynamic torque and frictional losses, self-starting dynamics, and runaway behavior. The latter is particularly important because, as reported for Wells turbines, a sudden loss of generator torque may lead to dangerous runaway speeds that cause excessive centrifugal stress, for which safety valves are often installed in the turbine duct to prevent overspeed conditions (Falcão et al., 2016; Rosati et al., 2022; Saad et al., 2018). Similarly, the prediction of runaway speed is critical to ensure the structural stability of turbine components and to support the safe operation of OWC power systems (Bahreini et al., 2023).

2.4. Irregular wave generation and OWC chamber response modeling

The sea conditions near Chagui-do, the western part of Jeju Island in the Republic of Korea, were considered for the wave profile generation. At the considered site, wave energy density varies between 1 and 4 kW/m throughout the year, while the significant wave height (H_s) varies between 0.5 and 1.1 m, and the mean wave period varies between 6 and

8 s (Hong et al., 2004, 2021). Here, H_s is defined as the average height of the highest one-third of waves observed. To characterize the irregular wave, the JONSWAP spectrum was utilized, which is defined by H_s and the peak spectral period T_p ($T_p \approx 1.12T_e$), where T_e is the wave energy period (Hasselmann et al., 1973). The angular frequency range ($\omega_f \in$ [0.2, 2.5] rad/s) was discretized into 50 linearly spaced components. A peak enhancement factor of 2.5 was utilized.

The energy flux of the waves per unit crest length in deep water, P_W, can be determined using Equation (6):

$$P_W = \frac{\rho_w g^2}{64\pi} H_s^2 T_e, \tag{6}$$

where ρ_w is the seawater density and g is the gravitational acceleration. The free surface elevation of the wave states was generated using MATLAB (Vazirizade, 2019). Based on this approach, several values of T_p and H_s were examined, specifically $T_p = 6.0$, 6.75, and 7.5 s, along with $H_s = 0.6$, 0.7, and 0.8 m. The elevation profiles were then scaled down by a factor of 1/16 to match the CFD model. Hence, in the CFD model, the corresponding values of T_p and H_s were 1.5, 1.69, and 1.88 s, and 0.0375, 0.0438, and 0.05m, respectively. In total, five cases were conducted, analyzed, and presented with specific operating conditions.

The spectral shape obtained by applying the fast Fourier transform to the wave train time series in Fig. 3a closely matched the spectrum generated using the JONSWAP empirical formula, as illustrated in Fig. 3b. The relative errors in the peak spectral value and the zeroth spectral moment were 13.96% and 4.17%, respectively, confirming that the generated irregular wave conditions are sufficiently accurate for use in subsequent analyses. Moreover, for the other generated wave cases, the relative errors of the peak spectral value and the zeroth spectral moment remained below 18% and 10%, respectively, further validating the reliability of the wave generation approach adopted in this study.

The governing equation proposed by Setoguchi et al. (1999) describes the dynamic relationship between the incident wave height H and the time-varying internal water surface elevation h inside the fixed OWC chamber:

$$\frac{d}{dt}\left(\rho_w h A_c \frac{dh}{dt}\right) = [\rho_w g(H-h) - \Delta p_c]A_c\ . \tag{7}$$

Here, A_c is the cross-sectional area of the air chamber, and Δp_c represents the internal air pressure deviation within the chamber. The left-hand side expresses the time derivative of the vertical water momentum inside the chamber, while the right-hand side denotes the net driving force, comprising the hydrostatic restoring force and the counteracting air pressure force. Equation (7) effectively governs the vertical motion of the internal free surface within the OWC chamber in response to H and Δp_c. To simplify the model, Δp_c was approximated as a functional relationship of the water surface velocity (dh/dt), expressed as $F(dh/dt)$. This assumption leads to the following second-order nonlinear differential equation:

$$h\frac{d^2h}{dt^2} + \left(\frac{dh}{dt}\right)^2 + F\left(\frac{dh}{dt}\right) - g(H-h) = 0\ . \tag{8}$$

It should be noted that the present formulation represents an approximation, as the governing equation of motion for OWC systems is commonly derived within the framework of linear wave theory (Folley and Whittaker, 2002). The resulting ordinary differential equation was numerically integrated using the Runge–Kutta–Gill scheme to obtain the time history of the internal free-surface elevation, $h(t)$, which serves as a

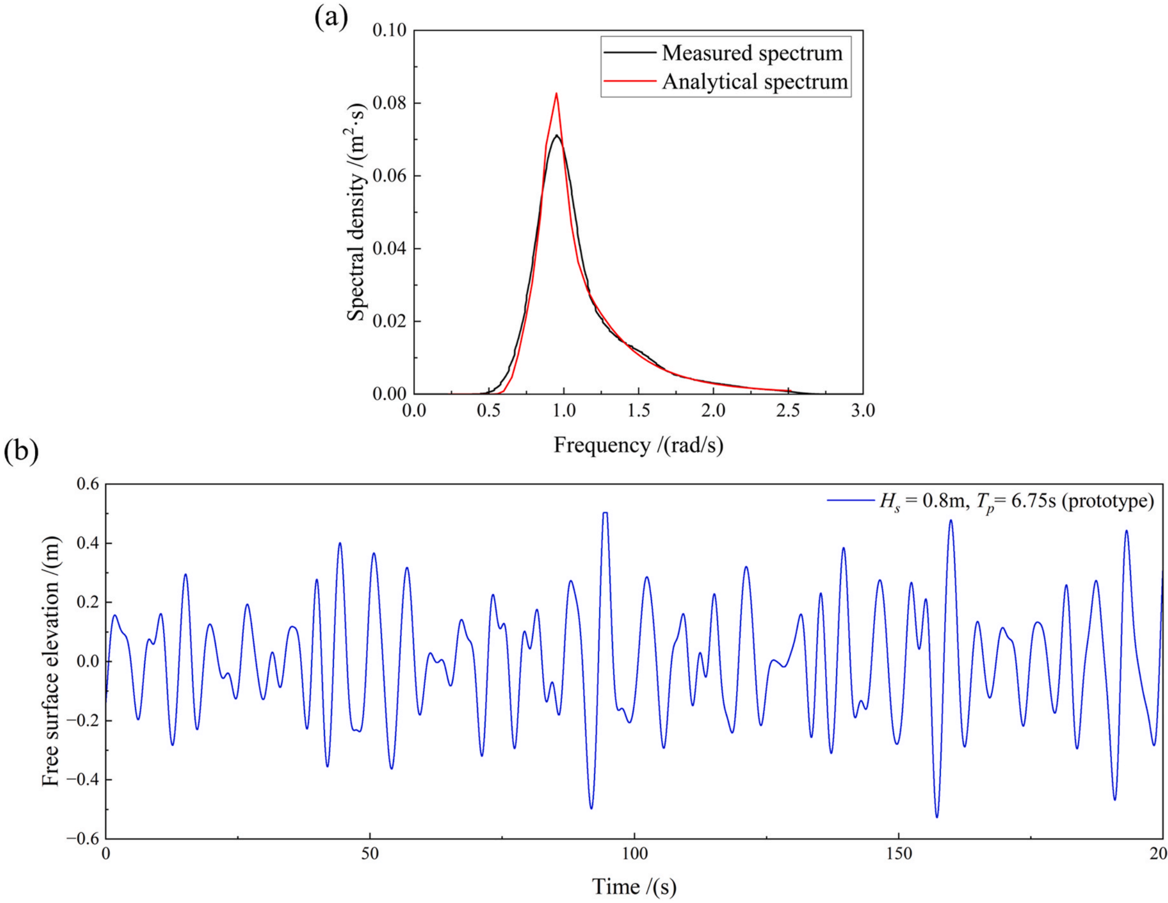

Fig. 3. Irregular wave condition of $H_s = 0.8$ m and $T_p = 6.75$ s for prototype: (a) comparison of analytical and generated JONSWAP spectrum, and (b) free surface elevation of the generated wave.

key input for modeling the airflow through the turbine (Inoue et al., 1986; Maeda et al., 2001). The computed variation of $h(t)$ was subsequently converted into an axial airflow velocity at the turbine inlet under the assumption of air incompressibility. In the present study, the chamber model is employed solely to prescribe unsteady inflow conditions representative of OWC operation, while chamber compressibility, duct inertia, and turbine–chamber coupling effects are intentionally excluded to isolate the intrinsic aerodynamic response and self-starting behavior of the turbine. Fig. 4 presents the resulting time histories of the free-surface elevation inside the chamber and the corresponding inflow velocity obtained from the numerical integration of the governing equation.

2.5. Dimensional analysis

The steady-state aerodynamic performance of the CFAT is evaluated using the dimensionless flow coefficient Φ, dimensionless pressure coefficient Ψ, and the dimensionless torque coefficient Π. They are defined as:

$$\Phi = \frac{Q}{\Omega D_1^3}, \Psi = \frac{\Delta p}{\rho \Omega^2 D_1^2}, \Pi = \frac{T_{\mathrm{turb}}}{\rho \Omega^2 D_1^5} \cdot [] \tag{9}$$

Here, Q is the volumetric flow rate, Δp is the pressure head between the nozzle inlet and outlet, and T_{turb} is the turbine torque. For the transient simulations in this study, these non-dimensional coefficients were adopted as:

$$\Phi^* = \frac{Q(t)}{\Omega(t) D_1^3}, \ \Psi^* = \frac{\Delta p(t)}{\rho \Omega(t)^2 D_1^2}, \Pi^* = \frac{T_{\mathrm{turb}}(t)}{\rho \Omega(t)^2 D_1^5}. \tag{10}$$

Here, Φ^*, Π^*, Ψ^* are the transient flow coefficient, transient pressure coefficient, and transient torque coefficient, respectively, where $Q(t)$, $\Delta p(t)$, and $T_{\mathrm{turb}}(t)$ represent instantaneous values of volumetric flow rate, pressure drop between the nozzle inlet and outlet, and torque, respectively. Mean instantaneous efficiency η^* was calculated using:

$$\eta^* = \frac{\sum_{t=t_0}^{t_N} T_{\mathrm{turb}}(t)\Omega(t)}{\sum_{t=t_0}^{t_N} \Delta p(t) Q(t)}. \tag{11}$$

Since an adaptive timescale was used for the transient simulations, the results were generated at non-uniform time intervals. Therefore, the composite trapezoidal rule was employed to calculate the time-averaged torque $\overline{T}_{\mathrm{turb}}$,

$$\overline{T}_{\mathrm{turb}} = \frac{1}{t_N - t_0} \sum_{i=0}^{N-1} \frac{T_{\mathrm{turb},i} + T_{\mathrm{turb},i+1}}{2} (t_{i+1} - t_i), \tag{12}$$

and time-averaged efficiency $\overline{\eta}$,

$$\overline{\eta} = \frac{\overline{P}_{\mathrm{turb}}}{\overline{P}_{\mathrm{pneu}}}. \tag{13}$$

Here, $\overline{P}_{\mathrm{turb}}$ and $\overline{P}_{\mathrm{pneu}}$ are the time-averaged turbine power and the time-averaged turbine available pneumatic power, respectively:

$$\overline{P}_{\mathrm{turb}} = \frac{1}{t_N - t_0} \sum_{i=0}^{N-1} \frac{T_i \Omega_i + T_{i+1}\Omega_{i+1}}{2} (t_{i+1} - t_i), \tag{14}$$

$$\overline{P}_{\mathrm{pneu}} = \frac{1}{t_N - t_0} \sum_{i=0}^{N-1} \frac{\Delta p_i Q_i + \Delta p_{i+1} Q_{i+1}}{2} (t_{i+1} - t_i). \tag{15}$$

Statistical quantities were evaluated using time-weighted formulations to ensure proper accounting of non-uniform sampling intervals. Accordingly, the weighted standard deviation ($\sigma_{T_{\mathrm{turb}}}$) and skewness ($\gamma_{1,T_{\mathrm{turb}}}$) of T_{turb} were computed as in Equations (16) and (17),

$$\sigma_{T_{\mathrm{turb}}} = \sqrt{\frac{1}{t_N - t_0} \sum_{i=0}^{N-1} \left(T_{\mathrm{turb},i} - \overline{T}_{\mathrm{turb}}\right)^2 (t_{i+1} - t_i)} \tag{16}$$

$$\gamma_{1,T_{\mathrm{turb}}} = \frac{1}{t_N - t_0} \frac{\sum_{i=0}^{N-1} \left(T_{\mathrm{turb},i} - \overline{T}_{\mathrm{turb}}\right)^3 (t_{i+1} - t_i)}{{\sigma_{T_{\mathrm{turb}}}}^3} \tag{17}$$

3. Results and discussion

3.1. Starting pattern with various inflow patterns

Three types of inflow conditions were considered to investigate the self-starting characteristics of the CFAT: steady unidirectional flow, bidirectional sinusoidal flow, and random irregular airflow generated from a wave spectrum. Each case was simulated for 35 s, with inflow parameters selected to ensure that the total volume input over the simulation period remained comparable across all scenarios. The steady inflow conditions were defined by a constant air velocity of 3 m/s. For the sinusoidal flow, an amplitude of 4.65 m/s and a wave period of 2 s were used, corresponding to the volume of the irregular wave case with an $H_s = 0.05$ m and $T_p = 1.69$ s. To ensure volumetric equivalence among the three conditions, the total air volume transferred over the 35 s was calculated as 1.260 m^3 for the steady inflow, 1.243 m^3 for the sinusoidal case, and 1.262 m^3 for the irregular wave, indicating less than 1.5% deviation across profiles. In all cases, the loading torque was set to zero to isolate the turbine's fundamental aerodynamic response, enabling a clear assessment of its self-starting behavior. Fig. 5 presents the time histories of the inlet flow velocity (Fig. 5a), rotor angular velocity (Fig. 5b), aerodynamic torque (Fig. 5c), and pressure differential across the turbine (Fig. 5d). The results demonstrate that the CFAT successfully initiated rotation under each of the inflow conditions, with

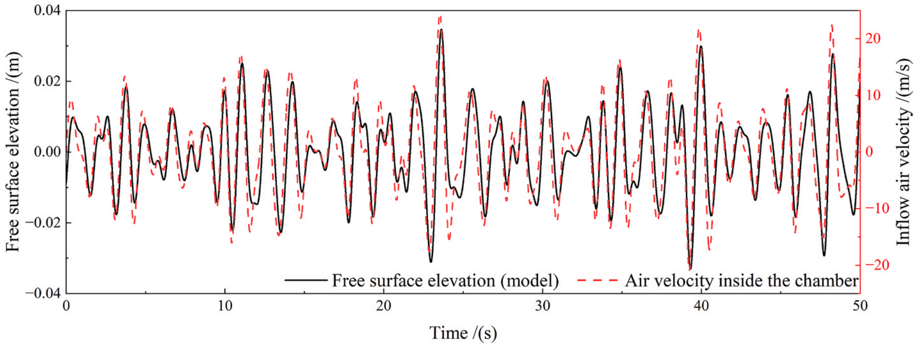

Fig. 4. Free surface elevation of $H_s = 0.05$ m and $T_p = 1.69$ s inside the chamber for model (black continuous line, left y-axis) and air velocity inside the chamber (red dashed line, right y-axis). (For interpretation of the references to colour in this figure legend, the reader is referred to the Web version of this article.)

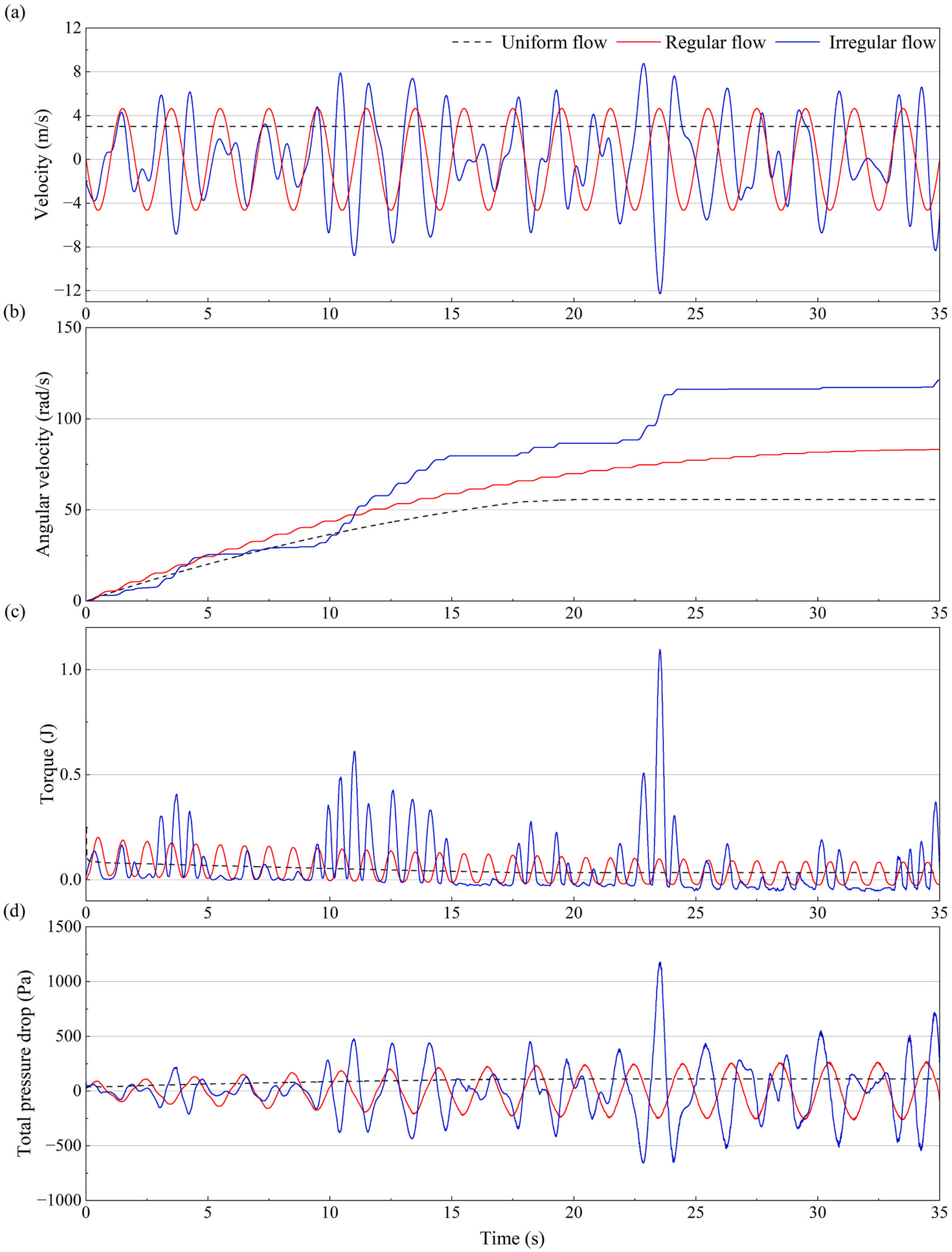

Fig. 5. Comparison of time histories of performance parameters: (a) air inflow velocity, (b) angular velocity of the CFAT, (c) generated pneumatic torque, and (d) total pressure drop across the rotor under different inflow patterns: uniform flow (black dashed line), regular flow (red), and irregular flow with $H_s = 0.05$ m and $T_p = 1.69$ s (blue). (For interpretation of the references to colour in this figure legend, the reader is referred to the Web version of this article.)

variations in transient response dynamics depending on the nature of the airflow.

In the uniform inflow case, the rotor experienced a steady but relatively slow acceleration, ultimately stabilizing at an angular velocity of approximately 90 rad/s after 19 s. For the regular sinusoidal flow, the CFAT accelerated more rapidly; however, it reached the equilibrium speed later (after 34 s) and then maintained a steady plateau thereafter. A comparable starting pattern has also been reported for impulse turbines operating under sinusoidal waves (Setoguchi et al., 2001). The irregular wave case exhibits slower and lower acceleration at the beginning, followed by step-like increases driven by wave group bursts, and later reaches a higher angular velocity. Even though the rotational speed did not reach equilibrium within the considered 35 s for the same total air volume input as the other two cases, the turbine did not exhibit any signs of poor starting ability, which has been reported for the Wells turbine under similar flow conditions (Cui et al., 2022). The extended behavior of this case beyond 35 s is discussed in Section 3.2.

The turbine produced a high initial torque during the acceleration phase, which gradually decayed as the rotor speed increased in the uniform inflow case. In the regular sinusoidal inflow, the torque response was strongly governed by the oscillatory nature of the air inflow. Although the maximum torque amplitude decreased with time, the response maintained a regular oscillatory pattern synchronized with the sinusoidal inflow. Within each wave cycle, the turbine consistently generated two distinct torque peaks, corresponding to the two extrema of the sinusoidal velocity: the inhalation and exhalation phases, also similar to the observations from the Wells turbine (Wang et al., 2024). Moreover, negative torques could be observed during the flow reversal phases due to insufficient flow to generate a positive torque with the corresponding rotational speed. In contrast, the irregular inflow produced a more complex response characterized by bursty fluctuations and intermittent peaks. This intermittent behavior limited acceleration and delayed the attainment of equilibrium rotational speed compared with the uniform and regular flow cases. During the initial stage, the pressure drop fluctuations did not immediately track the imposed airflow. In uniform and regular flow cases, a clear synchronization between the total pressure drop across the turbine and the inlet velocity emerged after approximately 10 s, once the rotor had accelerated and the internal flow structures had stabilized. The irregular case required a longer adjustment, with a comparable, repeatable pattern appearing only after about 12 s. Beyond that, the pressure drop was generally in phase with the inlet velocity for both the regular and irregular inflows. In the irregular case, pronounced pressure peaks occurred coincident with inflow surges, producing larger peak-to-valley excursions during energetic wave groups.

Fig. 6 presents the non-dimensional torque and pressure coefficients of the CFAT as functions of the flow coefficient under uniform, regular, and irregular inflow conditions. Fig. 6(a) and (b) correspond to the 2–8 s of operation, representing the starting behavior of the turbine, while Fig. 6(c and d) correspond to the dynamic equilibrium stage after the rotor has reached a stable rotational speed. During the self-starting stage, the uniform inflow case exhibits a smooth curve, indicating a quasi-steady response. Although the inflow velocity remains constant, variations of the turbine's angular velocity cause noticeable torque changes in the range $\Phi^* = -0.04$ to -0.1. For regular flow, the response follows a predictable periodic variation with respect to Φ^*. When subjected to irregular flow, the data scatter becomes much broader, especially in Fig. 6b. The irregular inflow induces pronounced cycle-to-cycle fluctuations, resulting in a noticeable spread and dispersion of the coefficients relative to the uniform flow curve. Importantly, the irregular data do not collapse onto a single path; instead, they form a diffuse band over the range of Φ^*. To further investigate the nature of this dispersion, the pressure coefficient data were conditionally averaged by separating inhalation and exhalation processes and binning the flow coefficient. This analysis reveals a clear and systematic separation between the two trajectories in the Ψ^*–Φ^* plane during the self-starting stage, indicating

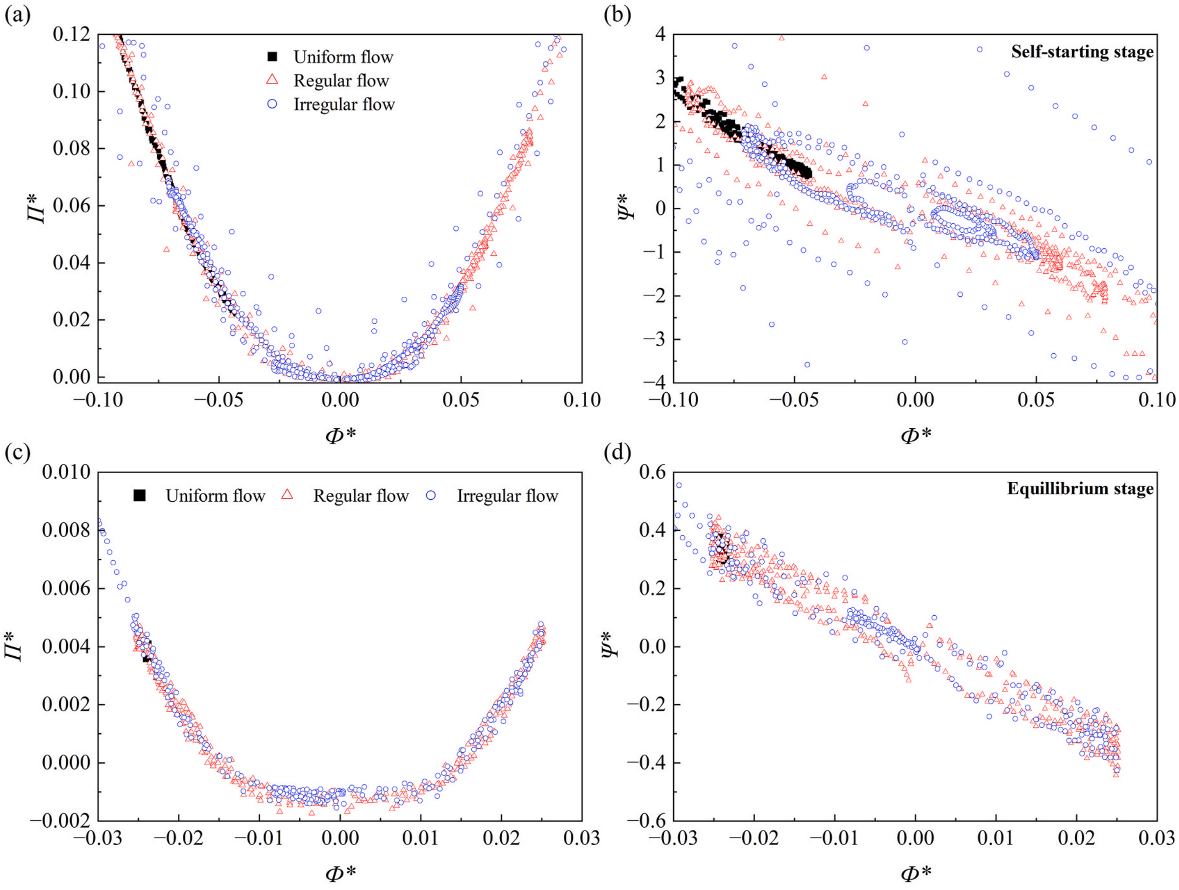

Fig. 6. Comparison of transient non-dimensional coefficients with respect to flow coefficient Φ^* under different inflow patterns: uniform flow (black solid square), regular flow (red open triangle), and irregular flow with $H_s = 0.05$ m and $T_p = 1.69$ s (blue open circle) at the self-starting stage: (a) torque coefficient Π^*, (b) pressure coefficient Ψ^*, and at the equilibrium stage: (c) torque coefficient Π^*, (d) pressure coefficient Ψ^*. (For interpretation of the references to colour in this figure legend, the reader is referred to the Web version of this article.)

the presence of hysteresis-like behavior in the pressure response. Notably, this separation is not limited to the transient startup phase. As shown in Fig. 6d, distinct inhalation and exhalation paths persist during the equilibrium stage, demonstrating that the hysteresis in the pressure–flow relationship remains under statistically steady operating conditions, whereas the steady flow results form a vertical line on the plots after reaching its stable angular velocity.

In contrast, the torque coefficient exhibits an essentially single-valued relationship with the flow coefficient in both stages, suggesting that the hysteresis primarily affects the pressure dynamics rather than the torque generation. This behavior indicates a form of persistent aerodynamic hysteresis associated with directional flow reversal and internal flow development, rather than stall-induced hysteresis commonly reported in Setoguchi et al. (2003). The CFD simulations analyzed by Cui et al. (2022) and Ghisu et al. (2017) clearly show hysteretic loops in the non-dimensional coefficients during dynamic stall of lift-based Wells turbines. The hysteresis observed here is therefore attributed to asymmetric pressure recovery and flow structures within the CFAT during inhalation and exhalation, which persist even after the rotor reaches dynamic equilibrium.

3.2. *Influence of significant wave height on CFAT performance*

Numerical simulations were performed under irregular wave conditions with varying significant wave heights for 80 s to evaluate the influence of wave intensity on the self-starting and early-stage operating characteristics of the CFAT. The analysis considered three key performance parameters: rotor angular velocity, aerodynamic torque on the runner at no-load condition, and pressure drop across the turbine. These parameters were examined over three distinct operating stages: the initial self-starting phase, the transition to steady rotation, and a short duration following the stabilization. The peak wave period was fixed at $T_p = 1.69$ s, and three irregular wave conditions with $H_s = 0.0375$, 0.0438, and 0.05 m were investigated.

Fig. 7(a–c) compare the generated inflow spectra with the analytical JONSWAP spectra for each wave height, showing excellent agreement in both peak frequency and spectral energy distribution. Fig. 7(d–g) present the corresponding time histories of inlet airflow velocity, rotor angular velocity, aerodynamic torque, and pressure drop across the runner, respectively. Across all simulations, increasing H_s resulted in stronger inflow oscillations and higher instantaneous airflow amplitudes. The inlet velocity profiles (Fig. 7d) exhibit typical wave-grouping patterns, where intermittent bursts of large velocity amplitudes are followed by short lull periods. This grouping behavior directly influences the rotor acceleration process. The comparison of angular velocities in Fig. 7e confirms that larger H_s values yield greater available pneumatic power and consequently higher rotational speeds. The $H_s = 0.0375$ m case shows a rapid initial acceleration during the first 20 s due to a series of energetic inflow events, reaching a moderate plateau near 120 rad/s by approximately 70 s. The $H_s = 0.0438$ m case exhibits a similar trend but attains a slightly higher equilibrium range of 135–145 rad/s. The highest-intensity case ($H_s = 0.05$ m) achieves the greatest peak speed of about 150 rad/s, but subsequently undergoes short-term fluctuations before settling near 140 rad/s toward the end of the simulation.

The simulations show that all three cases eventually approach a quasi-equilibrium rotational state, in which the mean angular velocity becomes nearly steady while minor oscillations persist owing to continuous inflow variability. Nevertheless, transient disturbances still occur within the equilibrium regime. In the $H_s = 0.05$ m case, a pronounced reduction in inflow amplitude between 50 s and 60 s temporarily decreases the aerodynamic loading. During this lull, the turbine continues to rotate by inertia, causing a short-term phase mismatch between the inflow and the blade incidence angle. As a result, localized flow reversal develops around the blade trailing edges, producing intermittent negative torque values. This behavior highlights the strong sensitivity of the CFAT to instantaneous inflow energy: when the inflow velocity (or, equivalently, the effective wave height) is reduced, the torque decreases proportionally and may briefly reverse under weak or disordered flow conditions.

Throughout the acceleration and steady phases, larger H_s values generate higher peak torques (Fig. 7f) corresponding to moments of strong inflow. However, they also lead to more frequent torque fluctuations and deeper negative torque events during flow reversals. Once quasi-steady rotation is achieved, the torque signal remains highly unsteady, reflecting persistent aerodynamic interactions between the periodic inflow and the rotor's inertia. The pressure drop across the runner (Fig. 7g) exhibits a similar oscillatory pattern to the inlet velocity but with an approximate $T_p/4$ phase lag, owing to the capacitive behavior of the OWC, also noted in Das et al. (2022). The amplitude increases markedly as H_s rises from 0.0375 m to 0.05 m. At the early stage, the total pressure oscillations are relatively small due to the low rotational speed. As the rotor accelerates, the amplitude of pressure oscillations increases and becomes synchronized with the airflow velocity, consistent with the observations reported by Wang et al. (2024) for the Wells turbine. This behavior confirms that the magnitude of the wave-induced airflow and the transient coupling between the chamber pressure and the rotor response govern the pneumatic loading on the CFAT.

Overall, the rotor dynamics are strongly modulated by the grouping of energetic waves and intermittent lull periods, which control the buildup and relaxation of aerodynamic torque. The results further confirm that higher wave intensity enhances energy conversion efficiency but also introduces larger torque variability, a trade-off characteristic of turbines operating in stochastic OWC environments.

Table 5 presents the time-averaged torque, power, and efficiency of the CFAT under different significant wave heights, separately evaluated using Equations (11)–(17) for the self-starting stage (0–40 s) and the dynamic equilibrium stage (40–80 s). The torque and power values are normalized to the unit spanwise length, with the span length in the present model set to 0.04 m. During the self-starting stage, the time-averaged torque and power increase monotonically with increasing H_s, reflecting the stronger pressure oscillations and enhanced aerodynamic forcing associated with larger wave heights. Specifically, the normalized mean torque rises from 1.33 J/m at $H_s = 0.0375$ m to 1.93 J/m at $H_s = 0.05$ m, accompanied by a corresponding increase in mean power from 71.9 W/m to 145.6 W/m. The associated efficiencies during the self-starting stage remain relatively high and weakly dependent on H_s, indicating that the turbine effectively converts intermittent airflow bursts into rotational acceleration during startup.

In contrast, the dynamic equilibrium stage exhibits a qualitatively different trend. While the mean power still increases with H_s, the time-averaged torque and efficiency are substantially lower than those observed during self-starting. Specifically, the normalized mean torque decreases to 0.55 J/m at $H_s = 0.0375$ m, 0.49 J/m at $H_s = 0.0438$ m, and 1.02 J/m at $H_s = 0.05$ m, with corresponding mean power levels of 62.6 W/m, 68.1 W/m, and 143.8 W/m, respectively, and efficiency values of 0.269, 0.223, and 0.285. This reduction is attributed to the balance between positive and negative torque contributions over each oscillation cycle, which becomes more pronounced at steady operation. The reduction at $H_s = 0.0438$ m is consistent with the transient torque histories in Fig. 7f, where, after approximately 45 s, the inflow weakened considerably, resulting in minimal productive torque despite the rotor's equilibrium speed. In contrast, at $H_s = 0.0375$ m and 0.05 m, the inflow retained sufficient oscillatory strength across the cycle, enabling steadier torque generation. The mean instantaneous efficiency levels were consistently higher than the time-averaged efficiencies, highlighting the role of short-duration peaks observed in Fig. 7(f) and (g). These results demonstrate that while higher wave heights deliver more absolute power, the conversion efficiency is strongly dependent on the temporal structure of the airflow, not simply its magnitude.

The transient aerodynamic behavior under varying significant wave heights was further examined through a frequency-domain analysis, in

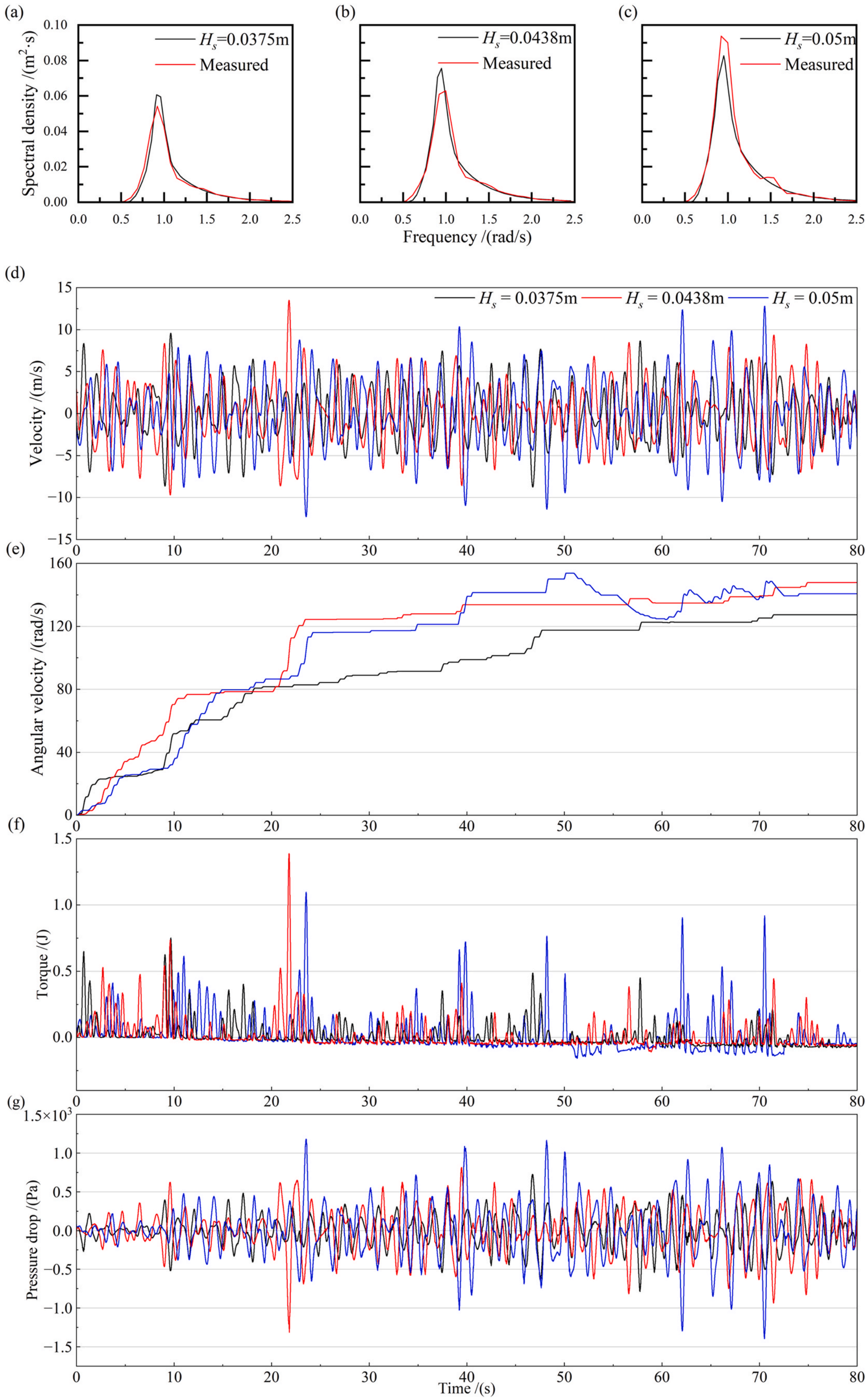

Fig. 7. Comparison of time histories of performance parameters: (a) air inflow velocity, (b) angular velocity of the CFAT, (c) generated torque, and (d) total pressure drop across the rotor under different significant wave heights: $H_s = 0.0375$ m (black), 0.0438 m (red), and 0.05 m (blue) at constant peak spectral period of $T_p = 1.69$ s. (For interpretation of the references to colour in this figure legend, the reader is referred to the Web version of this article.)

Table 5
Key performance results of the CFAT under different significant wave heights for the self-starting period (0–40 s) and dynamic equilibrium stage (40–80 s).

	H_s [m]	$\overline{T}_{\text{turb}}$ [J/m]	$\sigma_{T_{\text{turb}}}$	$\gamma_{1,T_{\text{turb}}}$	$\overline{P}_{\text{turb}}$ [W/m]	$\overline{\eta}$	η^*
Self-starting stage	0.0375	1.33	0.110	3.163	71.9	0.467	0.513
	0.0438	1.84	0.155	3.673	136.6	0.473	0.518
	0.05	1.93	0.149	2.754	145.6	0.478	0.512
Dynamic equilibrium stage	0.0375	0.55	0.077	2.976	62.6	0.269	0.316
	0.0438	0.49	0.069	2.936	68.1	0.223	0.243
	0.05	1.02	0.143	3.278	143.8	0.285	0.297

which the power spectral density (PSD) of the principal flow and performance variables was obtained. The results illustrate the spectrum of the instantaneous pressure drop across the runner of the CFAT (Fig. 8a), the torque (Fig. 8b), obtained from the time histories shown in Fig. 7. The PSD of the pressure drop exhibits a dominant peak at $1\omega_p = 3.72$ rad/s, reflecting the principal oscillatory component of the bidirectional inflow. Here, ω_p is the fundamental angular frequency defined as $2\pi/T_p$. The peak amplitude increases monotonically with H_s, consistent with the larger instantaneous pressure gradients generated by stronger airflow. A secondary broadening of the spectrum is observed for the highest H_s case, indicating enhanced modulation of the pressure difference due to the irregular grouping of air inflow.

The torque spectrum in Fig. 8b reveals a more complex structure with two characteristic secondary peaks, one near $0.25\omega_p$ and another at $2\omega_p$. The higher-frequency component at $2\omega_p$ originates from the torque exhibiting two peak responses within each wave cycle, corresponding to the bidirectional phases of the oscillating flow (Dorrell and Hsieh, 2008). The low-frequency feature near $0.25\omega_p$, which is absent under regular sinusoidal inflow, is attributed to slow phase modulation and amplitude drift associated with irregular wave-group envelopes and the transient startup process. To further examine the origin of this low-frequency feature, a flow-envelope analysis was performed on the torque time series. The extracted envelope isolates the slow amplitude modulation of the torque response and suppresses the carrier-scale oscillations associated with ω_p and its harmonics.

The PSD of the torque envelope exhibits a persistent peak near $0.25\omega_p$ during both the self-starting and dynamic equilibrium stages. The survival of this peak after demodulation confirms that it represents a genuine low-frequency modulation rather than a by-product of wave-scale oscillations or numerical artifacts. This modulation is attributed to the grouping of irregular waves, which induces slow variations in airflow intensity and sustained torque bursts spanning several wave periods.

A similar trend was reported by Liu et al. (2021) for an impulse turbine operating under regular-wave excitation, where the rotation speed and torque spectra showed distinct peaks at $1\omega_p$ and $2\omega_p$ due to the periodic alignment of pressure and flow oscillations. In contrast, the CFAT in this study was subjected to irregular wave-induced inflow, resulting in a secondary low-frequency feature ($\approx 0.25\omega_p$) instead of a sharp $1\omega_p$ peak. This difference highlights that, while both turbines share the $2\omega_p$ harmonic associated with alternating pressure extrema, the CFAT exhibits additional low-frequency modulation due to its sensitivity to inflow irregularity and its continuous self-rectifying operation.

3.3. *Influence of peak spectral period on CFAT performance*

The effect of the peak spectral period on the CFAT performance was examined by conducting simulations under three irregular wave conditions with $T_p = 1.5$, 1.69, and 1.88 s while maintaining a constant significant wave height of $H_s = 0.05$ m. The time series were normalized by each corresponding peak period ($t^* = t/T_p$) to facilitate direct comparison across conditions, and the analysis covered approximately 50 wave cycles. Fig. 9(a–c) compare the spectra of the simulated air inflow with the corresponding analytical JONSWAP spectra. The simulated inflows accurately reproduce the target spectral shapes, showing strong agreement in both peak frequency and spectral bandwidth. Fig. 9(d–g) illustrate the corresponding time histories of inlet airflow velocity, rotor angular velocity, aerodynamic torque, and pressure drop across the runner, respectively.

Variations in T_p substantially influence the temporal structure of the airflow (Fig. 9d). Shorter periods produce more frequent oscillations with reduced amplitude, while longer periods generate fewer but more energetic inflow bursts separated by extended lull intervals. These differences in the inflow characteristics directly influence the transient aerodynamic loading and, consequently, the start-up and early operational behavior of the turbine.

The angular velocity evolution in Fig. 9e shows that the CFAT successfully self-starts and accelerates under all three inflow conditions without exhibiting low-speed “crawling,” which commonly occurs in Wells turbines under bidirectional flow (Inoue et al., 1986; Wang et al., 2024). In the $T_p = 1.5$ s case, the turbine undergoes the most rapid initial acceleration, exceeding 100 rad/s within the first 20 s ($t^* \approx 13$). The $T_p = 1.69$ s and $T_p = 1.88$ s cases exhibit slower but smoother acceleration profiles. As the simulations progress to $t^* \approx 50$, all three cases reach a quasi-equilibrium rotational stage, maintaining nearly constant mean angular velocities of approximately 140–150 rad/s with small periodic fluctuations. This indicates that while the spectral period strongly influences the transient acceleration rate and the short-term torque response, its effect on the final steady-state rotational speed is comparatively minor.

The torque histories (Fig. 9f) mirror the temporal variations in inlet velocity, exhibiting intermittent positive bursts during each half-cycle of inhalation or exhalation. As the oscillation period shortens, torque peaks occur more frequently, leading to denser clusters of energy-transfer events. The $T_p = 1.5$ s case shows the highest occurrence of moderate-amplitude torque spikes, reflecting more continuous energy input from successive wave groups. Conversely, the $T_p = 1.88$ s case produces fewer but occasionally stronger peaks due to longer recovery intervals

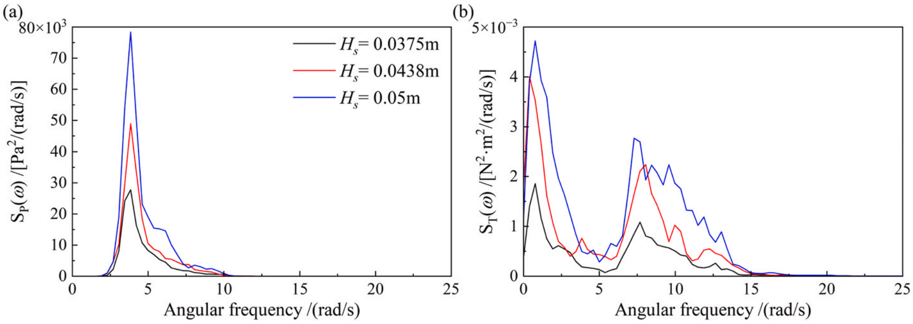

Fig. 8. Power spectral density of (a) pressure drop across the runner and (b) torque, under varying $H_s = 0.0375$, 0.0438, and 0.05 m at $T_p = 1.69$ s.

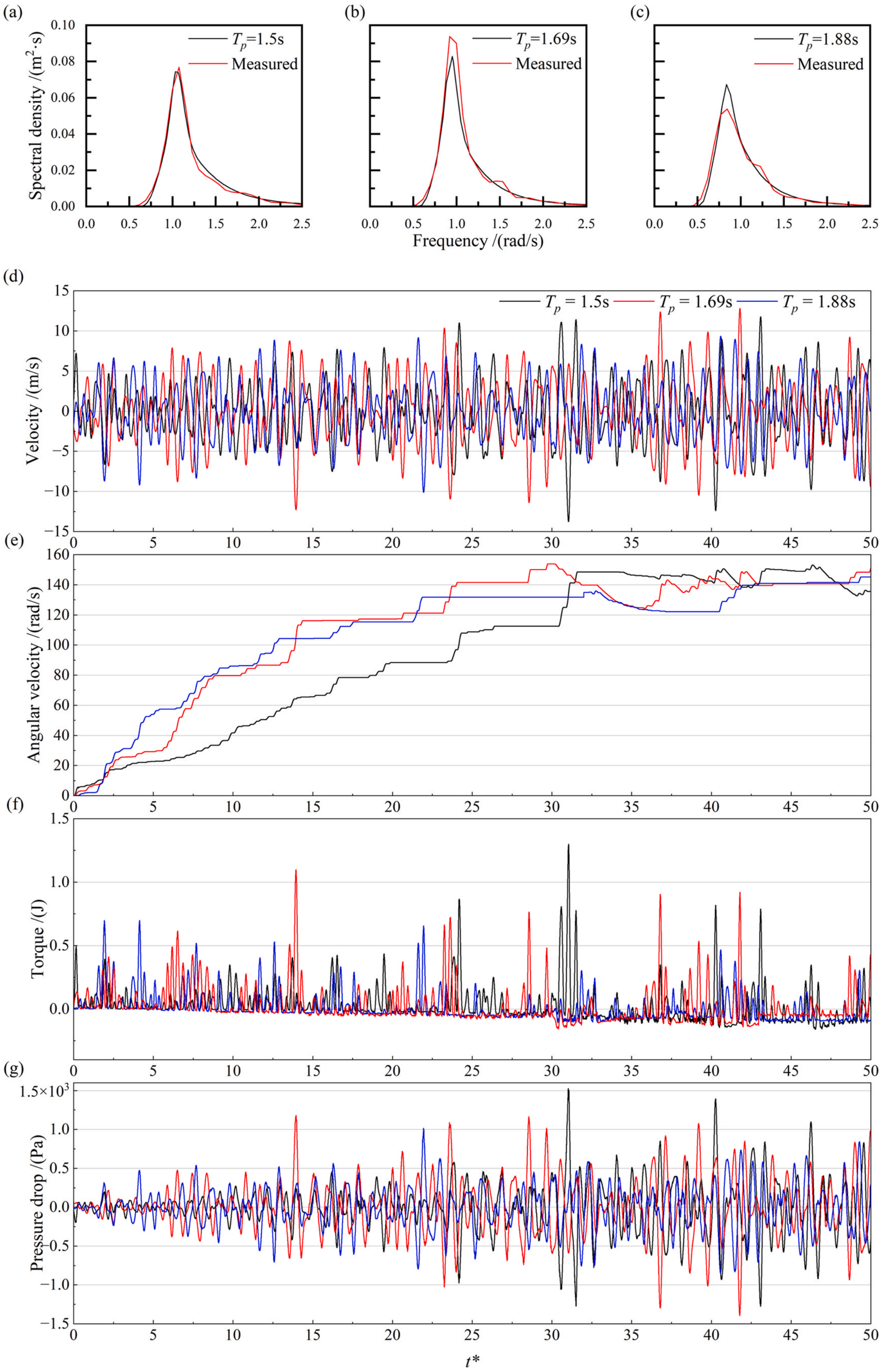

Fig. 9. Comparison of time histories of performance parameters: (a) air inflow velocity, (b) angular velocity of the CFAT, (c) generated torque, and (d) total pressure drop across the rotor under different peak spectral periods: $T_p = 1.5$ s (black), 1.69 s (red), and 1.88 s (blue) at constant significant wave height of $H_s = 0.05$ m. (For interpretation of the references to colour in this figure legend, the reader is referred to the Web version of this article.)

between energetic inflows. In all simulations, short negative torque intervals appear during flow reversals, corresponding to phases when the instantaneous aerodynamic loading becomes insufficient to overcome the rotor's inertial motion. These transient torque dips are less pronounced for shorter-period inflows, as the frequent alternation of jet direction allows quicker re-establishment of attached flow and momentum transfer.

The pressure drop across the turbine (Fig. 9g) oscillates almost in phase with the inlet velocity, confirming that the chamber pressure fluctuations dominate the aerodynamic forcing. As the rotor speed increases, the amplitude of pressure oscillations also grows, stabilizing once the equilibrium stage is reached. The magnitude of the peak-to-valley pressure difference is comparable among the three cases, though the shorter-period condition ($T_p = 1.5$ s) shows slightly smoother oscillations, indicating better synchronization between the airflow and the rotating passages.

The time-averaged performance metrics for varying peak spectral periods evaluated separately for the self-starting stage (0–40 s) and the dynamic equilibrium stage (40–80 s) are summarized in Table 6. During the self-starting stage, the turbine response shows a pronounced dependence on the spectral period. Among the cases considered, the highest mean torque and power are observed at $T_p = 1.69$ s, reaching 1.93 J/m and 145.6 W/m, respectively, compared with 1.47 J/m and 87.3 W/m at $T_p = 1.5$ s and 1.54 J/m and 96.5 W/m at $T_p = 1.88$ s. This enhanced performance at $T_p = 1.69$ s can be attributed to the presence of relatively strong wave groups during the early stage of the simulation, particularly between 5 and 15 s, which generate sustained high-amplitude airflow and promote effective torque build-up during rotor acceleration. The efficiencies during self-starting remain relatively high across all cases, with only modest variation among spectral periods, indicating that the CFAT can effectively convert intermittent airflow bursts into rotational acceleration over a broad range of wave conditions.

Once the turbine reaches dynamic equilibrium, the influence of the spectral period becomes more systematic. Shorter peak periods lead to more frequent airflow oscillations, which increase the continuity of torque production and reduce intervals of weak aerodynamic forcing. As a result, the time-averaged torque increases from 0.75 J/m at $T_p = 1.88$ s to 1.02 J/m at $T_p = 1.69$ s and further to 1.47 J/m at $T_p = 1.5$ s, accompanied by corresponding increases in mean power from 97.2 W/m to 143.8 W/m and 205.6 W/m. Equilibrium efficiency follows the same trend, reaching its maximum at $T_p = 1.5$ s, where the airflow provides a more consistent energy input over successive oscillation cycles. These findings indicate that while the self-starting behavior is strongly influenced by intermittent wave-group effects, the long-term performance of the CFAT is primarily controlled by the oscillation frequency of the incoming airflow.

3.4. Flow field analysis

The present flow-field analysis aims to establish a physical interpretation of the instantaneous performance trends presented in Sections 3.1–3.3 by elucidating the unsteady aerodynamic mechanisms responsible for torque fluctuations and efficiency variation. In particular, the instantaneous velocity and total pressure distributions at the center plane are examined for the case $H_s = 0.0438$ m and $T_p = 1.69$ s, over one oscillation cycle (43.5–45.2 s), to clarify how the pressure distribution leads to transient negative torque during flow reversals. Seven representative phases were selected for the analysis, such as inflow acceleration ‘i’, peak inflow ‘ii’, inflow deceleration ‘iii’, zero-crossing ‘iv’, outflow acceleration ‘v’, peak outflow ‘vi’, and outflow deceleration ‘vii’, as illustrated in Fig. 10.

Table 6
Key performance results of the CFAT under different peak spectral periods for the self-starting stage (0–40 s) and dynamic equilibrium stage (40–80 s).

	T_p [s]	$\overline{T}_{\text{turb}}$ [J/m]	$\sigma_{T_{\text{turb}}}$	$\gamma_{1,T_{\text{turb}}}$	$\overline{P}_{\text{turb}}$ [W/m]	$\overline{\eta}$	η^*
Self-starting stage	1.5	1.47	0.105	2.969	87.3	0.541	0.586
	1.69	1.93	0.149	2.754	145.6	0.478	0.512
	1.88	1.54	0.119	2.434	96.5	0.474	0.519
Dynamic equilibrium stage	1.5	1.47	0.177	3.117	205.6	0.335	0.364
	1.69	1.02	0.143	3.278	143.8	0.285	0.297
	1.88	0.75	0.101	2.998	97.2	0.276	0.307

Fig. 11 visualizes the velocity and pressure contours of the inflow stage. During this period, the airflow moves from left to right through the turbine domain. During inflow acceleration (Fig. 11a), a high-speed jet forms at the left nozzle lip and travels toward the right, attaching to the outer blade row, the outer region of the rotor where the jet first impinges before passing through the blade passages toward the inner blade row near the rotor. These outer and inner rows correspond to the two flow passages of the CFAT rotor, where the air crosses the blades twice within a single half-cycle. The total-pressure drop is concentrated just downstream of the nozzle, and only weak recirculation appears inside the runner, showing that energy transfer to the rotor is efficient at the start of the inflow phase.

At peak inflow, the velocity jet becomes stronger and passes smoothly through the blade passages toward the inner region (Fig. 11c). The pressure difference (Fig. 11d) between the outer and inner blade rows reaches its maximum, producing the first torque peak in the cycle described in Section 3.2. This phase represents the most effective conversion of airflow momentum into useful torque. Therefore, when the inflow velocity or, equivalently, the wave height is amplified, the torque increases proportionally, while a weaker inflow or smaller wave height results in a lower torque response. As the inflow weakens, the velocity decays (Fig. 11e), and the adverse pressure gradient (Fig. 11f) along the flow direction increases. Consequently, the jet begins to separate from the pressure-side trailing edges. Small recirculation zones develop near the inner passages, and the pressure drop across the blades decreases, leading to the torque reduction seen in the results. Under higher H_s conditions, the acceleration and deceleration are steeper, intensifying this temporary separation and creating short periods of reverse loading on the blades—consistent with the negative torque events noted in Section 3.2. In contrast, when T_p is shorter, the flow reverses more quickly, leaving less time for large vortices or separation to develop. The jet remains better attached to the blades across cycles, allowing smoother momentum exchange and higher average power output, as discussed in Section 3.3.

Fig. 12 shows the velocity and pressure contours at the zero-crossing phase, when the inflow direction ceases and the flow begins to reverse. At this instant, the airflow entering from the left side weakens and nearly collapses inside the runner (Fig. 12a), while the pressure field (Fig. 12b) displays residual vortical structures of opposite rotation in the two ducts. Small, localized flow reversals appear near the nozzle lips, and the pressure gradient across the rotor almost vanishes. Consequently, the aerodynamic torque drops to nearly zero or slightly negative values,

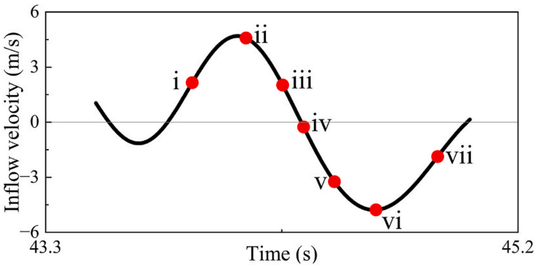

Fig. 10. Seven representative phases used for flow field analysis from the case $H_s = 0.0438$ m and $T_p = 1.69$ s: i) inflow acceleration, ii) peak inflow, iii) inflow deceleration, iv) zero-crossing, v) outflow acceleration, vi) peak outflow, and vii) outflow deceleration.

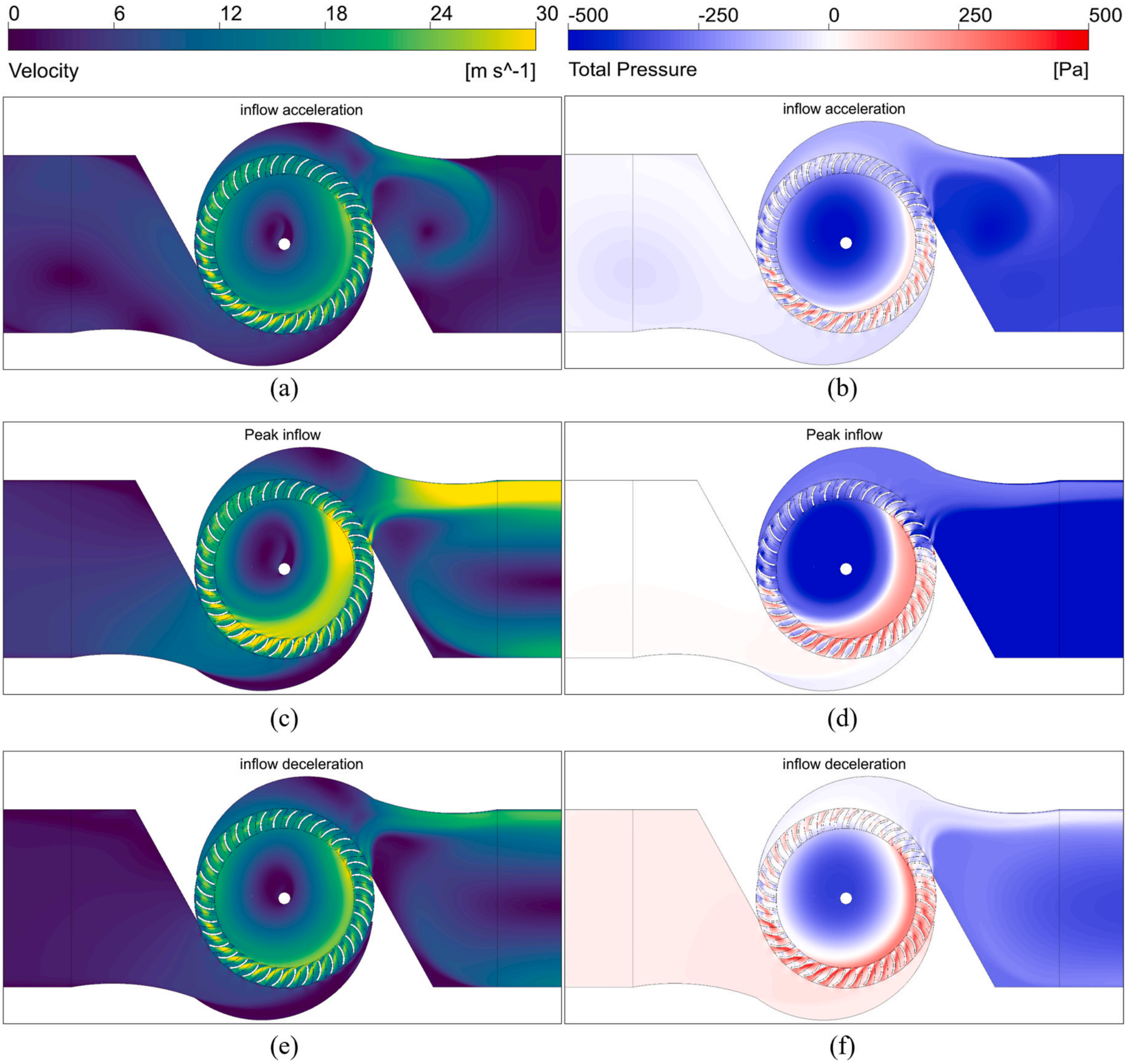

Fig. 11. Velocity and pressure contours at the center plane of the CFAT inflow within a single airflow cycle from the $H_s = 0.0438$ m and $T_p = 1.69$ s case (43.5–45.2 s). The velocity contours: (a) inflow acceleration, (c) peak inflow, and (e) inflow deceleration. The pressure contours: (b) inflow acceleration, (d) peak inflow, and (f) inflow deceleration.

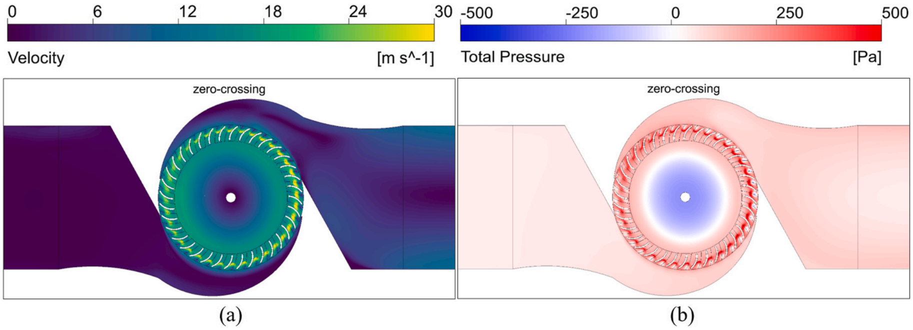

Fig. 12. Velocity and pressure contours at the center plane of the zero-crossing stage within a single airflow cycle from the $H_s = 0.0438$ m and $T_p = 1.69$ s case (43.5–45.2 s): (a) velocity and (b) pressure contours.

which corresponds to the short interval of inertial rotor motion described in Sections 3.2 and 3.3. The appearance of counter-rotating vortices at the zero-crossing indicates that flow energy is momentarily stored as rotational motion within the rotor passages rather than being transmitted to useful torque.

Fig. 13 presents the velocity and total pressure contours during the outflow stage, in which the airflow reverses direction, entering from the right-side nozzle and exiting to the left through the turbine passages. The velocity contours (Fig. 13a) exhibit asymmetric filling due to remnants of the inflow structures, while pressure recovery (Fig. 13b)

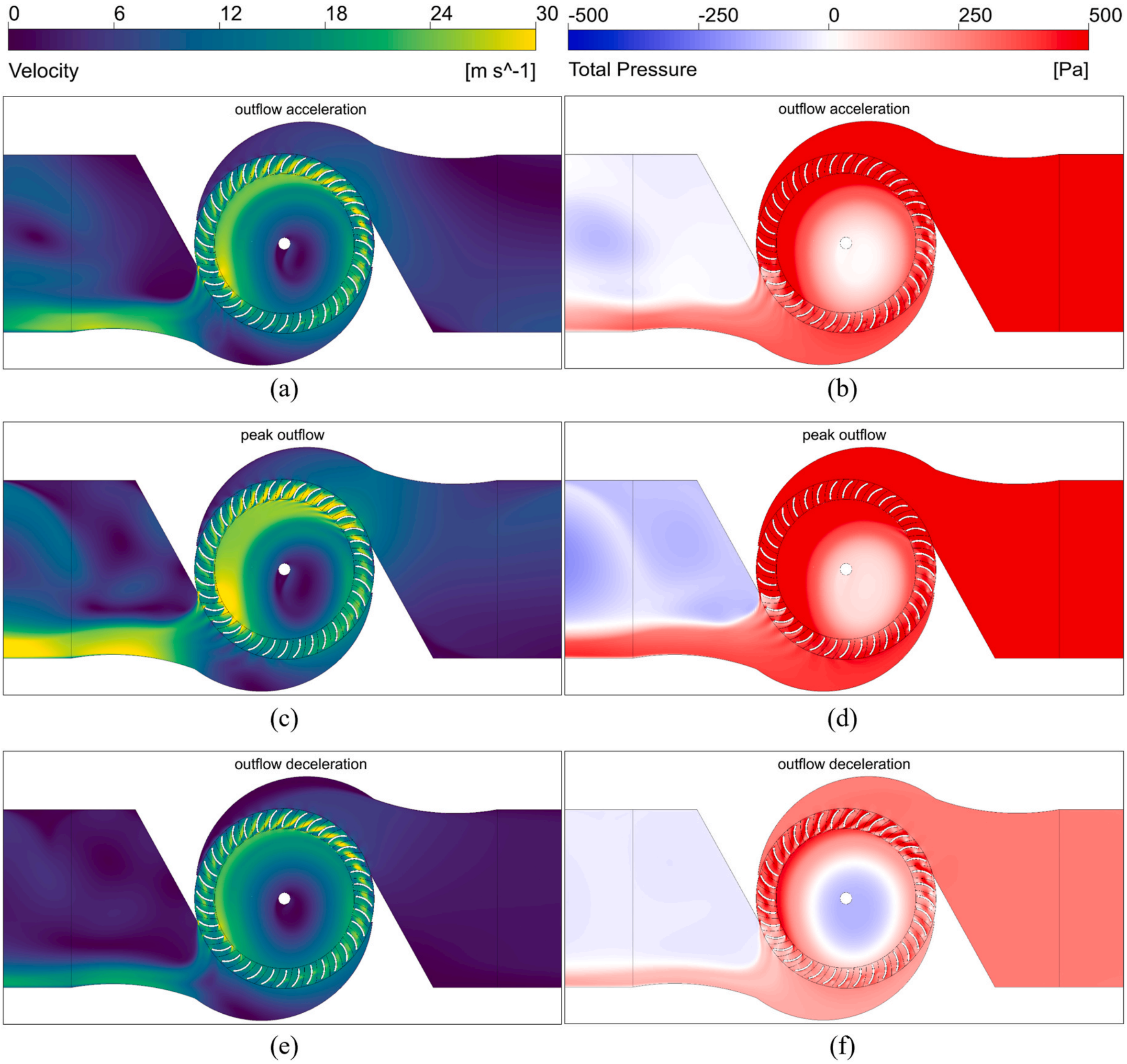

Fig. 13. Velocity and pressure contours at the center plane of the CFAT outflow within a single airflow cycle from the $H_s = 0.0438$ m and $T_p = 1.69$ s case (43.5–45.2 s). The velocity contours: (a) outflow acceleration, (c) peak outflow, and (e) outflow deceleration. The pressure contours: (b) outflow acceleration, (d) peak outflow, and (f) outflow deceleration.

progresses across the newly active passages. Torque recovers rapidly, emphasizing the turbine's ability to adapt to reversal without a full stall event. At peak outflow, the reversed jet mirrors the inflow peak, with high-velocity ribbons fully occupying the blade passages (Fig. 13c). Meanwhile, total pressure gradients across the runner are strongest (Fig. 13d). This stage corresponds to the second major torque peak, confirming that the CFAT maintains nearly symmetric performance under both flow directions. Accordingly, an increase in the reversed inflow velocity, or equivalently, in the effective H_s leads to a proportional rise in torque, whereas a smaller wave height produces a reduced torque response. Finally, as the outflow diminishes, the jet dissipates and enlarged recirculation regions dominate both the velocity (Fig. 13e) and pressure fields (Fig. 13f). Losses increase in the diffuser and blade exits, marking the approach to the next zero-crossing.

Fig. 14 illustrates the distributions of spanwise vorticity, turbulence kinetic energy (TKE), and turbulence eddy dissipation at three characteristic instants of the oscillation cycle: peak inflow, zero-crossing, and peak outflow. As a fundamental feature of CFAT operation, the rotor preserves unidirectional rotation even under bidirectional excitation. Accordingly, negative vorticity relative to the present axis is predominantly observed near the rotor blades, except at the zero-crossing instant (Fig. 14a–c). A detailed comparison of the vorticity and turbulence kinetic energy fields is presented to further quantify their variation and relative contributions during the oscillation cycle.

The vorticity was computed from the instantaneous velocity gradients $(\nabla \times \widetilde{u})$, where $\widetilde{u} = (\widetilde{u}, \widetilde{v}, \widetilde{w})$ is the instantaneous velocity. The spanwise vorticity component was defined as $\omega_z = (\partial\widetilde{v}/\partial x) - (\partial\widetilde{u}/\partial y)$. The TKE corresponds to the modeled turbulent kinetic energy ($k = 0.5 u_i u_i$) predicted by the SST k-ω turbulence model, representing the energy of unresolved turbulent fluctuations.

During peak inflow, strong TKE is concentrated near the nozzle exit (Fig. 14d), where sharp velocity gradients are generated by the accelerating jet. This indicates that turbulence production is dominated by nozzle dynamics, and consequently, turbulence-induced noise (Fig. 14g) is expected to be most pronounced at the nozzle under these conditions. At the zero-crossing, however, a distinct shift occurs: strong positive vorticity emerges around the rotor (Fig. 14b), accompanied by a sharp rise in TKE dissipation along the blade surfaces (Fig. 14e). Most of the turbulent energy is dissipated in the blade passages, revealing that this instant is critical for turbulence–structure interactions. While the present isothermal model neglects thermal coupling, such localized dissipation (Fig. 14h) could raise blade surface temperatures in practical

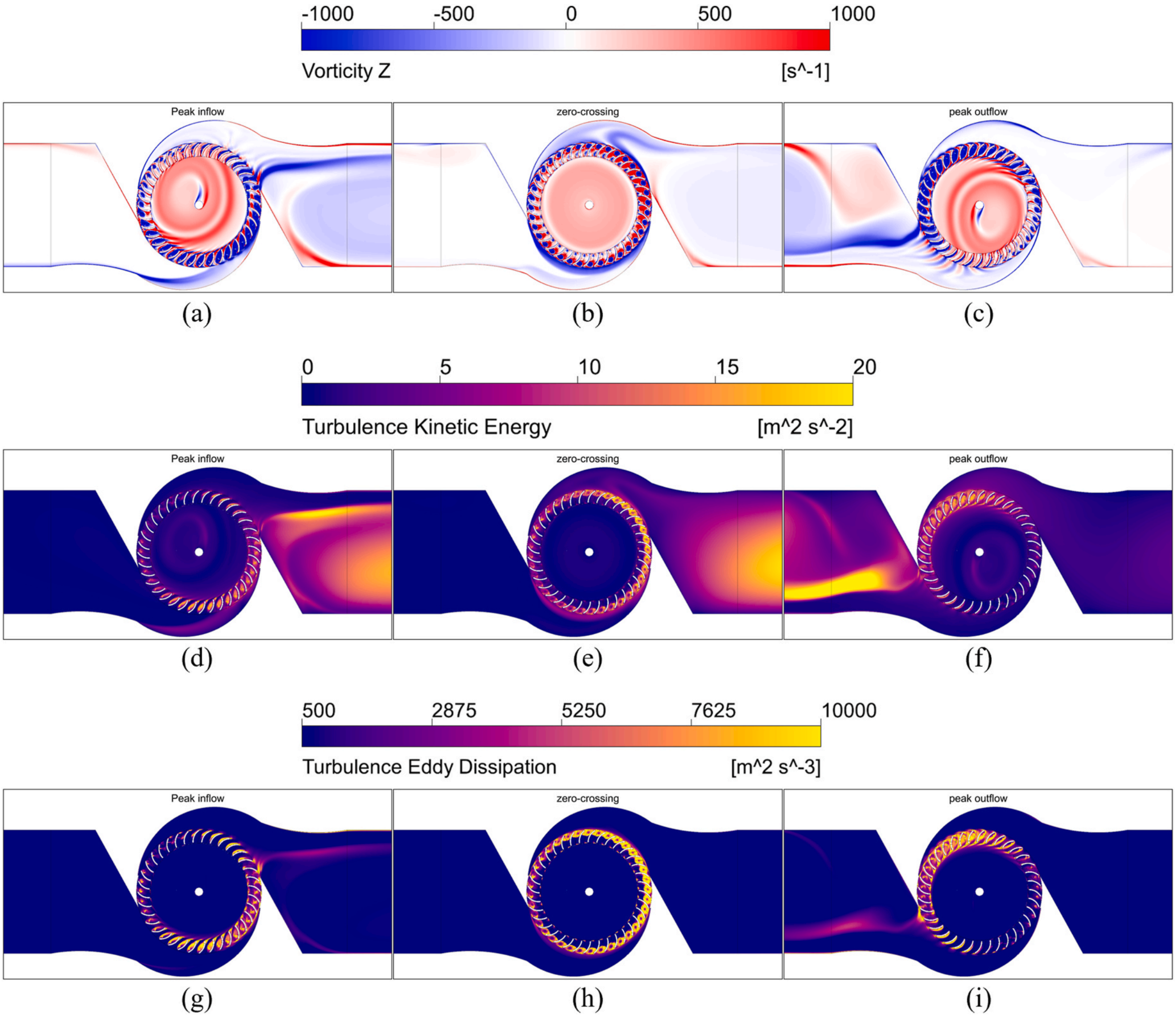

Fig. 14. Turbulence characteristics and vorticity contours at the center plane of the CFAT from the case with $H_s = 0.0438$ m and $T_p = 1.69$ s at three representative stages within a single airflow cycle: peak inflow, zero-crossing, and peak outflow. The selected instances are shown as: (a–c) spanwise vorticity, (d–f) turbulence kinetic energy, and (g–i) turbulence eddy dissipation.

operation, with implications for fatigue resistance. The steep spatial gradients in TKE around the rotor also suggest that turbulence-induced noise would primarily originate from the blade region during flow reversals (Piccolo et al., 2024; Zhang and Huang, 2023). Finally, during peak outflow, the turbulence distribution (Fig. 14f–i) again resembles the inflow phase, with intense TKE concentrated downstream of the nozzle jet. This confirms that nozzle-dominated turbulence is re-established once the flow direction stabilizes.

3.5. *Limitations of the study*

The present study is subject to several modeling and numerical limitations that should be considered when interpreting the results. The airflow was modeled as incompressible, and the pneumatic spring effect associated with the compressible air volume inside the OWC chamber was not explicitly resolved; instead, a simplified ordinary-differential-equation-based inflow model was employed to prescribe irregular airflow. While this approach captures the dominant wave-induced oscillatory characteristics, it may not fully represent pressure–flow coupling and resonance effects present in a fully coupled OWC system. However, these are not expected to alter the qualitative self-starting mechanisms and transient trends identified in the present study. The simulations were conducted under zero-load (free-spinning) conditions, and thus the reported torque dynamics reflect intrinsic aerodynamic behavior rather than performance under generator loading. In addition, the unsteady flow was resolved using a URANS framework with the SST k–ω turbulence model, which, although computationally efficient, has known limitations in capturing highly transient separated flows and cycle-to-cycle variability under strongly irregular inflow. A single realization of the irregular wave signal was considered for each sea state, and no formal statistical convergence or numerical uncertainty quantification was performed. Furthermore, adaptive time stepping was adopted to enable long-duration simulations, introducing potential uncertainty in resolving high-frequency torque fluctuations. Finally, due to computational cost constraints, the total simulation time was limited to 80 s (approximately 50 wave cycles), which is sufficient to distinguish self-starting and dynamic equilibrium behavior but may be insufficient for full low-frequency statistical convergence. Accordingly, the findings should be interpreted as a physics-based investigation of transient aerodynamic response under idealized irregular airflow rather than a comprehensive assessment of long-term performance in a fully coupled OWC–turbine system.

4. Conclusions

This study investigated the self-starting behavior and dynamic performance of a CFAT under irregular wave conditions using a fully transient CFD model. A free-spinning numerical approach was adopted to capture the natural acceleration of the rotor without external control. The initial analysis compared the CFAT start-up under three inflow profiles—uniform steady flow, regular sinusoidal flow, and irregular wave-induced flow—each delivering similar air volume. The turbine successfully self-started in all cases and exhibited hysteretic behavior in regular and irregular inflow cases under no-load conditions. Among the three conditions, the equilibrium state was reached fastest under steady inflow, followed by regular sinusoidal flow and then irregular waves. While the irregular case showed stronger fluctuations in pressure and non-dimensional coefficients, the turbine still achieved stable operation after several oscillation cycles, confirming its robust self-starting capability.

The effects of two key wave parameters were also examined by generating irregular inflows from a JONSWAP spectrum. For fixed $T_p = 1.69$ s, three significant wave heights ($H_s = 0.0375$ m, 0.0438 m, and 0.05 m) were simulated. Higher wave heights produced higher torque, power, and efficiency, consistent with trends observed in Wells and impulse turbines. A frequency-domain analysis of the transient responses further clarified the underlying aerodynamic behavior of the CFAT under irregular inflows. The pressure-drop spectrum exhibited a dominant peak near the fundamental wave frequency, reflecting the primary oscillatory motion of the bidirectional airflow. In contrast, the torque spectrum revealed two distinct components: a higher-frequency peak near $2\omega_p$ and a low-frequency component around $0.25\omega_p$. The former originates from the two torque maxima generated within each full wave cycle, whereas the latter is attributed to slow amplitude modulation and phase drift caused by irregular wave grouping and startup transients. These spectral features highlight that the CFAT's aerodynamic response is governed not only by the fundamental inflow frequency but also by nonlinear interactions and envelope effects inherent to irregular wave excitation. The influence of peak spectral period was then investigated for $T_p = 1.5$ s, 1.69 s, and 1.88 s at $H_s = 0.05$ m. Shorter wave periods enhanced torque and power output due to more frequent energetic inflow events, while efficiency depended strongly on the phasing of gust groups within the averaging window.

The internal flow fields were analyzed at seven representative stages within one oscillation cycle, namely inflow acceleration, peak inflow, inflow deceleration, zero-crossing, outflow acceleration, peak outflow, and outflow deceleration. The velocity and pressure contours revealed the evolution of jet development and wake recovery, while turbulence kinetic energy, dissipation, and vorticity fields highlighted phase-dependent turbulence production. The results confirm that the CFAT is a robust and efficient candidate for oscillating water column applications. The flow-field analyses further clarify the unsteady aerodynamics governing its operation, reinforcing its potential as a practical alternative to conventional OWC turbines.

Any change in the external load condition is inherently linked to variations in the internal flow characteristics; hence, establishing the aerodynamic baseline under zero-load conditions provides a necessary reference for future load-coupled simulations. While this assumption constitutes a limitation of the present study, the baseline analysis nevertheless provides essential insight into the intrinsic aerodynamic stability and transient response of the self-rectifying air turbine. It also forms a foundation for subsequent analyses incorporating generator damping and realistic load effects.

CRediT authorship contribution statement

B.H.B.P.D. Baddegamage: Writing – original draft, Validation, Investigation, Formal analysis. **Seong Jong Bae:** Visualization, Methodology, Data curation. **S.D.G.S.P. Gunawardane:** Writing – review & editing, Visualization, Methodology. **Young-Ho Lee:** Resources, Funding acquisition, Conceptualization. **Kilwon Kim:** Methodology, Funding acquisition, Data curation. **Min Yoon:** Writing – review & editing, Supervision, Project administration, Conceptualization.

Declaration of competing interest

The authors declare that they have no known competing financial interests or personal relationships that could have appeared to influence the work reported in this paper.

Acknowledgements

This research was supported by the Korea Institute of Marine Science & Technology Promotion (KIMST), funded by the Ministry of Oceans and Fisheries, Korea (RS-2023-00254688).

References

Babintsev, I.A., 1975. Apparatus for converting sea wave energy into electrical energy (United States Patent No. US3922739A). https://patents.google.com/patent/US3922739A/en.

Baddegamage, B.H.B.P.D., Bae, S.J., Jang, S.H., Gunawardane, S.D.G.S.P., Lee, Y.-H., Kim, K., Yoon, M., 2025. Performance improvement of a cross-flow air turbine for oscillating water column wave energy converter by nozzle and blade optimization. Ocean Eng. 316, 119986. https://doi.org/10.1016/j.oceaneng.2024.119986.

Baddegamage, B.H.B.P.D., Lee, Y.-H., Gunawardane, S.D.G.S.P., Yoon, M., 2024. Performance improvement of crossflow air turbines for wave energy conversion in oscillating water columns: a CFD study. In the SLIIT International Conference on Engineering and Technology. https://doi.org/10.54389/DLPQ3739.

Bae, S.J., Baddegamage, B.H.B.P.D., Jang, S.H., Kim, K., Yoon, M., 2026. Contributions of the blade and rotor design on the performance of a biradial turbine in oscillating water columns. Ocean Eng. 343, 123528. https://doi.org/10.1016/j.oceaneng.2025.123528.

Bahreini, A., Riasi, A., Quaranta, E., Nourbakhsh, A., 2023. Numerical and experimental study of a very low head (VLH) turbine in an open channel at no-load conditions. Sustain. Energy Technol. Assessments 60, 103429. https://doi.org/10.1016/j.seta.2023.103429.

Balasubramanian, R., Barrows, S., Chen, J., 2008. Investigation of shear-stress transport turbulence model for turbomachinery applications. In: 46th AIAA Aerospace Sciences Meeting and Exhibit. https://doi.org/10.2514/6.2008-566.

CFX-Solver, ANSYS, 2019. Theory guide. Release 19.2, 298.

Cruz, J., 2007. Ocean Wave Energy: Current Status and Future Prespectives. Springer Science & Business Media.

Cui, Y., Liu, Z., Wang, R., Hyun, B.-S., Zhang, Y., 2022. Numerical study on free-spinning performance of oscillating water column Wells turbine in reciprocating airflows. Phys. Fluids 34 (11), 115123. https://doi.org/10.1063/5.0122956.

Cui, Y., Liu, Z., Zhang, X., Xu, C., Shi, H., Kim, K., 2019. Self-starting analysis of an OWC axial impulse turbine in constant flows: experimental and numerical studies. Appl. Ocean Res. 82, 458–469. https://doi.org/10.1016/j.apor.2018.11.014.

Curran, R., Folley, M., 2008. Air turbine design for OWCs. In: Ocean Wave Energy—Current Status and Future Prospects. Springer, pp. 189–219.

Das, T.K., Kerikous, E., Venkatesan, N., Janiga, G., Thévenin, D., Samad, A., 2022. Performance improvement of a Wells turbine through an automated optimization technique. Energy Convers. Manag. 16, 100285. https://doi.org/10.1016/j.ecmx.2022.100285.

Ding, Z., Ning, D., Mayon, R., 2025. Wave-to-wire model for an oscillating water column wave energy converter. Appl. Energy 377, 124663. https://doi.org/10.1016/j.apenergy.2024.124663.

Dorrell, D.G., Hsieh, M.-F., 2008. Performance of Wells turbines for use in small-scale oscillating water columns. ISOPE International Ocean and Polar Engineering Conference. ISOPE-I. In: https://onepetro.org/ISOPEIOPEC/proceedings-abstract/ISOPE08/All-ISOPE08/10667.

Doyle, S., Aggidis, G.A., 2019. Development of multi-oscillating water columns as wave energy converters. Renew. Sustain. Energy Rev. 107, 75–86. https://doi.org/10.1016/j.rser.2019.02.021.

Falcão, A.F.O., 2025. Comparisons between self-rectifying air turbines and self-rectifying water turbines for OWC wave energy converters. Energy 335, 138161. https://doi.org/10.1016/j.energy.2025.138161.

Falcão, A.F.O., Gato, L.M.C., Nunes, E.P.A.S., 2013a. A novel radial self-rectifying air turbine for use in wave energy converters. Renew. Energy 50, 289–298. https://doi.org/10.1016/j.renene.2012.06.050.

Falcão, A.F.O., Gato, L.M.C., Nunes, E.P.A.S., 2013b. A novel radial self-rectifying air turbine for use in wave energy converters. Part 2. Results from model testing. Renew. Energy 53, 159–164. https://doi.org/10.1016/j.renene.2012.11.018.

Falcão, A.F.O., Henriques, J.C.C., 2016. Oscillating-water-column wave energy converters and air turbines: a review. Renew. Energy 85, 1391–1424. https://doi.org/10.1016/j.renene.2015.07.086.

Falcão, A.F.O., Henriques, J.C.C., Gato, L.M.C., 2016. Air turbine optimization for a bottom-standing oscillating-water-column wave energy converter. J. Ocean Eng. Marine Energy 2 (4), 459–472. https://doi.org/10.1007/s40722-016-0045-7.

Falcão, A.F.O., Henriques, J.C.C., Gato, L.M.C., 2018. Self-rectifying air turbines for wave energy conversion: a comparative analysis. Renew. Sustain. Energy Rev. 91, 1231–1241. https://doi.org/10.1016/j.rser.2018.04.019.

Folley, M., Whittaker, T.J., 2002. Identification of non-linear flow characteristics of the LIMPET shoreline OWC. The Twelfth International Offshore and Polar Engineering Conference.

Ghafoorian, F., Enayati, E., Mirmotahari, S.R., Wan, H., 2024a. Self-starting improvement and performance enhancement in Darrieus VAWTs using auxiliary blades and deflectors. Machines 12 (11), 806. https://doi.org/10.3390/machines12110806.

Ghafoorian, F., Mirmotahari, S.R., Wan, H., 2024b. Numerical study on aerodynamic performance improvement and efficiency enhancement of the savonius vertical axis wind turbine with semi-directional airfoil guide vane. Ocean Eng. 307, 118186. https://doi.org/10.1016/j.oceaneng.2024.118186.

Ghisu, T., Puddu, P., Cambuli, F., 2015. Numerical analysis of a Wells turbine at different non-dimensional piston frequencies. J. Therm. Sci. 24 (6), 535–543. https://doi.org/10.1007/s11630-015-0819-6.

Ghisu, T., Puddu, P., Cambuli, F., Virdis, I., 2017. On the hysteretic behaviour of Wells turbines. Energy Proc. 126, 706–713. https://doi.org/10.1016/j.egypro.2017.08.303.

Hasselmann, K., Barnett, T.P., Bouws, E., Carlson, H., Cartwright, D.E., Enke, K., Ewing, J.A., Gienapp, A., Hasselmann, D.E., Kruseman, P., Meerburg, A., Müller, P., Olbers, D.J., Richter, K., Sell, W., Walden, H., 1973. Measurements of wind-wave growth and swell decay during the joint North Sea wave project (JONSWAP). Ergänzungsheft Zur Deutschen Hydrographischen Zeitschrift. *Reihe A*. https://pure.mpg.de/pubman/faces/ViewItemOverviewPage.jsp?itemId=item_3262854.

Heath, T.V., 2012. A review of oscillating water columns. Philos. Trans. R. Soc. A Math. Phys. Eng. Sci. 370 (1959), 235–245. https://doi.org/10.1098/rsta.2011.0164.

Hong, J.-S., Moon, J.-H., Kim, T., Cho, I.-H., Choi, J., Park, J.Y., 2021. Response of wave energy to tidal currents in the western sea of Jeju Island, Korea. Renew. Energy 172, 564–573. https://doi.org/10.1016/j.renene.2021.03.052.

Hong, K.-Y., Ryu, H.-J., Shin, S.-H., Hong, S.-W., 2004. Wave energy distribution at Jeju sea and investigation of optimal sites for wave power generation. J. Ocean Eng. Technol. 18 (6), 8–15.

Hu, Q., Li, Y., 2017. Unsteady RANS simulations of Wells turbine under transient flow conditions. J. Offshore Mech. Arctic Eng. 140 (1), 011901. https://doi.org/10.1115/1.4037696.

Inoue, M., Kaneko, K., Setoguchi, T., Raghunathan, S., 1986. Simulation of starting characteristics of the Wells turbine. In: 4th Joint Fluid Mechanics, Plasma Dynamics and Lasers Conference. https://doi.org/10.2514/6.1986-1122.

Kang, H.-G., Kim, B.-H., Lee, Y.-H., 2017. A performance study of a cross-flow air turbine utilizing an orifice for OWC WEC. Koean Soc. Fluid Mach. J. Fluid Mach. 20 (3), 54–62. https://doi.org/10.5293/kfma.2017.20.3.054.

Kang, H.-G., Lee, Y.-H., Kim, C.-J., Kang, H.-D., 2022. Design optimization of a cross-flow air turbine for an oscillating water column wave energy converter. Energies 15 (7), 2444. https://doi.org/10.3390/en15072444.

Lacombe, F., Pelletier, D., Garon, A., 2019. Compatible wall functions and adaptive remeshing for the k-omega SST model. In: AIAA Scitech 2019 Forum. https://doi.org/10.2514/6.2019-2329.

Liu, Z., Cui, Y., Xu, C., Shi, H., Kim, K., 2018. Transient simulation of OWC impulse turbine based on fully passive flow-driving model. Renew. Energy 117, 459–473. https://doi.org/10.1016/j.renene.2017.10.095.

Liu, Z., Cui, Y., Xu, C., Sun, L., Li, M., Jin, J., 2019. Experimental and numerical studies on an OWC axial-flow impulse turbine in reciprocating air flows. Renew. Sustain. Energy Rev. 113, 109272. https://doi.org/10.1016/j.rser.2019.109272.

Liu, Z., Xu, C., Kim, K., 2021. Overall performance of a model OWC system under the free-spinning mode: an experimental study. Ocean Eng. 227, 108890. https://doi.org/10.1016/j.oceaneng.2021.108890.

Liu, Z., Xu, C., Kim, K., 2022. A CFD-based wave-to-wire model for the oscillating water column wave energy convertor. Ocean Eng. 248, 110842. https://doi.org/10.1016/j.oceaneng.2022.110842.

Lopes, B.S., Gato, L.M.C., Falcão, A.F.O., Henriques, J.C.C., 2019. Test results of a novel twin-rotor radial inflow self-rectifying air turbine for OWC wave energy converters. Energy 170, 869–879. https://doi.org/10.1016/j.energy.2018.12.078.

López, I., Iglesias, G., 2014. Efficiency of OWC wave energy converters: a virtual laboratory. Appl. Ocean Res. 44, 63–70. https://doi.org/10.1016/j.apor.2013.11.001.

Luo, Y., Tao, R., Peng, G., 2022. Comparative numerical study of the dynamic motion of OWC impulse turbine in the starting process. Ocean Eng. 245, 110429. https://doi.org/10.1016/j.oceaneng.2021.110429.

Lyu, X., Mi, C., Collions, S., Chen, W., Yang, D., Huang, L., 2025. Design and experimental tests for novel shapes of floating OWC wave energy converters with the additional purpose of breakwater. Ocean Eng. 328, 121031. https://doi.org/10.1016/j.oceaneng.2025.121031.

Maeda, H., Setoguchi, T., Takao, M., Sakurada, K., Kim, T.-H., Kaneko, K., 2001. Comparative study of turbines for wave energy conversion. J. Therm. Sci. 10 (1), 26–31. https://doi.org/10.1007/s11630-001-0005-x.

Menter, F.R., 1994. Two-equation eddy-viscosity turbulence models for engineering applications. AIAA J. 32 (8), 1598–1605. https://doi.org/10.2514/3.12149.

Menter, F.R., Kuntz, M., Langtry, R., others, 2003. Ten years of industrial experience with the SST turbulence model. Turbulence Heat Mass Trans. 4 (1), 625–632.

Pereiras, B., Castro, F., Marjani, A.E., Rodríguez, M.A., 2011. An improved radial impulse turbine for OWC. Renew. Energy 36 (5), 1477–1484. https://doi.org/10.1016/j.renene.2010.10.013.

Piccolo, A., Zamponi, R., Avallone, F., Ragni, D., 2024. Turbulence distortion and leading-edge noise. Phys. Fluids 36 (12), 125183. https://doi.org/10.1063/5.0244627.

Qiao, D., Haider, R., Yan, J., Ning, D., Li, B., 2020. Review of wave energy converter and design of mooring system. Sustainability 12 (19), 8251. https://doi.org/10.3390/su12198251.

Quaranta, E., Perrier, J.P., Revelli, R., 2022. Optimal design process of crossflow Banki turbines: literature review and novel expeditious equations. Ocean Eng. 257, 111582. https://doi.org/10.1016/j.oceaneng.2022.111582.

Rosati, M., Henriques, J.C.C., Ringwood, J.V., 2022. Oscillating-water-column wave energy converters: a critical review of numerical modelling and control. Energy Convers. Manag. 16, 100322. https://doi.org/10.1016/j.ecmx.2022.100322.

Saad, M., Pereiras, B., González, J., Oro, J.M.F., Díaz, M.G., 2018. Performance curve of a radial flow turbine for an OWC plant. Proceedings 2 (23), 1413. https://doi.org/10.3390/proceedings2231413.

Setoguchi, T., Kinoue, Y., Kim, T.H., Kaneko, K., Inoue, M., 2003. Hysteretic characteristics of Wells turbine for wave power conversion. Renew. Energy 28 (13), 2113–2127. https://doi.org/10.1016/S0960-1481(03)00079-X.

Setoguchi, T., Santhakumar, S., Maeda, H., Takao, M., Kaneko, K., 2001. A review of impulse turbines for wave energy conversion. Renew. Energy 23 (2), 261–292. https://doi.org/10.1016/S0960-1481(00)00175-0.

Setoguchi, T., Takao, M., 2006. Current status of self rectifying air turbines for wave energy conversion. Energy Convers. Manag. 47 (15), 2382–2396. https://doi.org/10.1016/j.enconman.2005.11.013.

Setoguchi, T., Takao, M., Kinoue, Y., Kaneko, K., Santhakumar, S., Inoue, M., 1999. Study on an impulse turbine for wave energy conversion. Int. J. Offshore Polar Eng. 10 (2), 145–152.

Shehata, A.S., Xiao, Q., Saqr, K.M., Alexander, D., 2017. Wells turbine for wave energy conversion: a review. Int. J. Energy Res. 41 (1), 6–38. https://doi.org/10.1002/er.3583.

Vazirizade, S.M., 2019. An Intelligent Integrated Method for Reliability Estimation of Offshore Structures Wave Loading Applied in Time Domain. The University of Arizona.

Veigas, M., López, M., Iglesias, G., 2014. Assessing the optimal location for a shoreline wave energy converter. Appl. Energy 132, 404–411. https://doi.org/10.1016/j.apenergy.2014.07.067.

Wang, R., Cui, Y., Liu, Z., Li, B., Zhang, Y., 2024. Numerical study on unsteady performance of a Wells turbine under irregular wave conditions. Renew. Energy 225, 120255. https://doi.org/10.1016/j.renene.2024.120255.

Wata, J., Kang, H.-G., Lee, Y.-H., 2016. Numerical analysis of a cross flow air turbine for oscillating water column plants. In the Korean Society of New and Renewable Energy Conference.

Wata, J., Lee, Y.-H., 2015. CFD simulation of a full scale OWC plant with a cross flow air turbine. In the Korean Society of Fluid Machinery Conference.

Wells, A., 1976. Fluid driven rotary transducer. British Patent Spec. 1, 595–700.

Zhang, J., Huang, Z., 2023. Transient flow and noise characteristics of accelerated flow past a hydrofoil with special emphasis on vortex-turbulence-noise interaction. Ocean Eng. 268, 113427. https://doi.org/10.1016/j.oceaneng.2022.113427.